Title: Novel quantal analysis method reveals conservation of injected charge by excitatory synapses across cortical cells of different sizes

Author Names and Affiliations: Martynas Dervinis[1], Guy Major[1]

[1]: Cardiff University, Cardiff, Wales, CF10 3AT, UK

Corresponding author email address: martynas.dervinis@gmail.com

Number of pages: 39

Number of figures: 9

Number of words

Abstract: 252

Body text excluding Materials and Methods: 3061

Conflict of interest statement: The authors declare no competing financial interests.

Acknowledgements: Cardiff University (GM, MD), The Medical Research Council of the UK (MD PhD). Neural activity simulations were performed on the Cardiff School of Biosciences' Biocomputing Hub HPC/Cloud infrastructure.

Abstract

In chemical synapses of the central nervous system (CNS), information is transmitted via the presynaptic release of a vesicle (or 'quantum') of neurotransmitter, which elicits a postsynaptic electrical response with an amplitude termed the 'quantal size'. This key determinant of neural computation is hard to measure reliably due to its small size and the multiple sources of noise within neurons and electrophysiological recordings. Measuring amplitudes of miniature postsynaptic currents (mPSCs) or potentials (mPSPs) at the cell soma potentially offers a technically straightforward way to estimate quantal sizes, as each of these miniature responses (or 'minis') is elicited by the spontaneous release of a single neurotransmitter vesicle. However, a somatically recorded mini is typically massively attenuated compared with at its input site, and a significant fraction are indistinguishable from (or cancelled out by) background noise fluctuations. Here we describe a novel quantal analysis method that estimates electrical size of the synapse by combining separate somatic recordings of background physiological noise and minis with simulations. With the help of a genetic algorithm, simulations are successfully used to infer the combined amplitude and rise time distribution of minis that would otherwise be inaccessible due to low signal to noise ratio. The estimated distributions reveal a striking inverse dependence of mean minis' amplitudes on cell's total capacitance (a proxy for the size of cells) that firmly supports the conservation of the electrical size of excitatory cortical synapses in rats. We incorporate the novel quantal analysis method into our patch clamp data analysis software called 'minis'.

45 # Abbreviations

46 ABF – Axon Binary File

47 aCSF – artificial cerebrospinal fluid

48 AMPA – α-amino-3-hydroxy-5-methyl-4-isoxazolepropionic acid

49 ANN – artificial neural network

50 AP – action potential

51 CPP – (*RS*)-3-(2-carboxypiperazin-4-yl)-propyl-1-phosphonic acid

52 EPSC – excitatory postsynaptic current

53 EPSP – excitatory postsynaptic potential

54 GA – genetic algorithm

55 GABA – gamma-aminobutyric acid

56 IPSC – inhibitory post-synaptic current

57 IPSP – inhibitory post-synaptic potential

58 MAD – maximal absolute deviation

59 mEPSC– miniature excitatory post-synaptic current

60 mEPSP– miniature excitatory post-synaptic potential

61 mIPSP– miniature inhibitory post-synaptic potential

62 mPSC – miniature post-synaptic current

63 mPSP – miniature post-synaptic potential

64 NBQX – 2,3-dioxo-6-nitro-1,2,3,4-tetrahydrobenzo[*f*]quinoxaline-7-sulfonamide

65 NMDA – N-methyl-D-aspartate

66 SAD – sum of absolute deviations

67 SD – standard deviation

68 smEPSP – simulated mEPSP

69 TTX – tetrodotoxin

70 V_m – membrane potential

Introduction

Synaptic transmission in the CNS occurs in 'quanta' (Forti et al., 1997; Hardingham et al., 2010; Isaacson and Walmsley, 1995; Jonas et al., 1993; Kraszewski and Grantyn, 1992; Kullmann and Nicoll, 1992; Kuno, 1964; Larkman et al., 1991; Sahara and Takahashi, 2001; Stern et al., 1992; Wall and Usowicz, 1998) usually thought to correspond to the release of a single neurotransmitter vesicle (Heuser et al., 1979). The amplitude of the postsynaptic response to a quantum of transmitter, the quantal size, is a key parameter defining the efficacy of synaptic transmission (Katz, 1969; Vere-Jones, 1966) and, therefore, an important determinant of neural computation.

Quantal size measurements in the CNS are difficult due to multi-synaptic contacts, limited accessibility, significant quantal variance, temporal non-stationarity of synaptic properties, and low signal-to-noise ratios of somatic electrophysiological recordings of quantal events (Bekkers, 1994; Korn and Faber, 1991). For these reasons classical quantal analysis as done at the neuromuscular junction has run into problems in central synapses. More recent methods such as noise deconvolution, Variance-Mean analysis, and optical quantal analysis have not fared much better either (Biró et al., 2005; Clamann et al., 1991; Clements, 2003; Clements and Silver, 2000; Edwards et al., 1976; Enoki et al., 2009; Jack et al., 1981; Liu et al., 2022; Oertner et al., 2002; Peled and Isacoff, 2011; Redman, 1990; Reid and Clements, 1999; Silver, 2003; Yuste et al., 1999).

A complementary method of assessing synaptic function is to measure properties of mPSCs. Miniature PSC amplitude measurements are often taken as quantal size estimates across the population of active synapses onto a neuron, as the mPSC (under voltage clamp) or mPSP (under voltage recording) likely correspond to the response to a spontaneous release of a single neurotransmitter vesicle (Brown et al., 1979; del Castillo and Katz, 1954; Fatt and Katz, 1952; Isaacson and Walmsley, 1995; Wall and Usowicz, 1998). Measurements of mPSC amplitudes are

96 routine in the literature. However, they are likely overestimates due to small amplitude events being
97 difficult to detect and largely being missed.
98
99 The use of voltage clamp can be a major reason why mPSCs “go missing”. Theoretical studies (Major,
100 1993; Rall and Segev, 1985; Spruston et al., 1993) predicted and experimental findings (Williams and
101 Mitchell, 2008) confirmed that voltage clamp fails to clamp extended dendrites, and to capture the
102 current flowing in at electrically remote synapses. Amplitude attenuation can also be caused if series
103 resistance is not compensated (Williams and Mitchell, 2008). These issues can be somewhat
104 sidestepped by switching to voltage recording.
105
106 However, most mPSCs go undetected because of the electrophysiology of the neuron itself. Distal
107 minis leak charge via the dendritic membrane, but an even more significant amplitude attenuation,
108 40-fold or more, is inflicted by charging the membrane capacitance of dendritic trees (Larkum et al.,
109 2009; Major et al., 2013a; Nevian et al., 2007; Stuart and Spruston, 1998; Williams and Mitchell,
110 2008; Williams and Stuart, 2002). Such amplitudes, at the soma, are often indistinguishable from
111 noise fluctuations. Recording from thin dendrites close to synaptic input sites is technically
112 challenging (Nevian et al. 2007). Therefore, a reliable yet widely accessible quantal analysis method,
113 based on somatic whole-cell patch recording, would require taking account of the background noise
114 component in addition to measuring putative mPSPs (or mPSCs).
115
116 Here we describe such a method based on separate recordings of excitatory mPSPs (mEPSPs) in the
117 presence of background physiological noise (‘noise + minis’ recording) and of noise alone after
118 blocking mEPSPs pharmacologically (‘noise-alone’ recording). To detect mEPSP-like events in these
119 recordings we used a newly developed algorithm called ‘minis’ which is described in our companion
120 article (Dervinis and Major, 2023). Because of larger minis overshadowing smaller potentials, events
121 detected in the ‘noise-alone’ recording cannot be used to account for the noise component in the

122 ‘noise + minis’ recording. Instead, simulated minis must be used by superimposing them on the
123 ‘noise-alone’ recording until the ‘noise + simulated minis’ voltage trace closely matches the ‘noise +
124 real minis’ recording. Therefore, we augmented ‘minis’ software with a genetic optimisation
125 algorithm (GA) that automatically adjusts amplitude and rise times of a simulated minis. The novel
126 quantal analysis method produced an unbiased quantal size estimate for excitatory synapses in the
127 CNS which was approximately equal to 28.53 pC and was conserved across pyramidal cells of all sizes
128 in cortical layers 2/3 and 5. ‘Minis’ thus provides a straightforward quantal analysis method of
129 detecting mPSPs and mPSCs in somatic recordings and separating smaller of these events from
130 background noise fluctuations.
131

132 Materials and Methods

133 **Animals and electrophysiology**

134 All experimental procedures were carried out in accordance with the UK Animals (Scientific
135 Procedures) Act 1986 at the Cardiff University under Home Office personal and project licenses. The
136 full description of electrophysiology procedures is provided in our companion article (Dervinis and
137 Major, 2023). Briefly, coronal somatosensory cortical slices obtained from 19- to 27-day old Wistar
138 rats (RRID:RGD_13508588; n = 11) of either sex were used to obtain whole-cell recordings (n = 14) of
139 mEPSPs in the background of physiological noise (‘noise + minis’ condition) by applying artificial
140 cerebrospinal fluid (aCSF) solution added with an action potential (AP) and inhibitory postsynaptic
141 potential (IPSP) blockers. Following this phase, the recordings were continued further after adding
142 excitatory postsynaptic potential (EPSP) blockers (‘noise-alone’ condition).
143

144 Passive membrane time constant, total capacitance, and cell’s input resistance (the bridge balance
145 error) were estimated by injecting current pulses as described in (Major G et al., 1993).
146

147 **Experimental design**

148 The goal of the study was to design a quantal analysis method based on somatic recordings of minis.
149 Due to low signal to noise ratio, simulations of minis were used to infer the signal component and to
150 eliminate the noise component in these recordings.

151

152 The experimental design of this study was similar to the one described in our companion article
153 (Dervinis and Major, 2023). As described in the previous section, two types of whole-cell recordings
154 were obtained where mEPSPs were recorded in the background of physiological noise or where
155 mEPSPs were pharmacologically blocked and only noise was recorded. The noise recordings were
156 then superimposed with simulated mEPSPs (smEPSPs) and 'minis' algorithm was applied to this
157 'noise + simulated minis' voltage trace. The resulting distribution of detected events in terms of their
158 amplitudes and 10-90% rise times was compared to the equivalent distribution based on 'noise +
159 real minis' recording. Discrepancy between the two distributions was used to inform the GA which
160 would then adjust the distribution of smEPSPs and generate new 'noise + simulated minis' voltage
161 traces and compare them again to the equivalent distribution based on 'noise + real minis'
162 recording. This procedure was repeated multiple times until the two distributions were closely
163 matched. At the end of this process the minis' distribution used for simulating a closely matched
164 recording was deemed to be the inference of the true minis' distribution underlying the 'noise + real
165 minis' recording.

166

167 **Detection of miniature postsynaptic potentials**

168 Detection of real and simulated mEPSPs was carried out using 'minis' software. The detailed
169 description of this detection algorithm is provided in our companion article (Dervinis and Major,
170 2023). We used the same detection algorithm parameters as described in that article except for the
171 amplitude range which was set to 0.02-10 mV.

172

173 **Selection of recordings for fitting distributions of detected real minis-like events**

174 Prior to carrying out any estimation of minis' distribution, segments of 'noise + real minis' and
175 'noise-alone' recordings were carefully selected. Segments containing unusual amount of noise or V_m
176 glitches were rejected. Parts of recording showing instability or drift of recording parameters were
177 also rejected to ensure that only good quality data was used. We called this a preprocessing stage
178 and data analyses we performed at this stage were inbuilt into 'minis' software.

179

180 As part of the preprocessing stage 'minis' produced 7 graphs showing the evolution of various
181 recording parameters across the entire duration of a single recording. An example is provided in
182 Figure 1 showing these graphs as individual panels of the figure for the longest obtained recording.
183 Figure 1A shows the evolution of V_m from the very beginning of the recording obtained in the regular
184 aCSF with APs present to the very end of the recording where APs as well as mEPSPs and mIPSPs
185 were blocked for some time ('noise-alone' recording phase). The data is shown after removing V_m
186 segments containing pulses with the total duration of 8519.9 s. Throughout the entirety of this
187 recording the baseline V_m varied between –70 and –67 mV and, thus remained relatively stable.

188

189 There are 3 time markers that extend across all figure panels marking the time when the aSCF
190 containing TTX and gabazine was infused to block APs and IPSPs (the first marker), the time when
191 APs were observed to cease (the second marker), and the time when the aCSF containing NBQX and
192 CPP was infused to block remaining EPSPs (the third marker). The recording segment between the
193 second and the third markers constituted the 'noise + minis' recording, while the segment following
194 the third marker when mEPSPs were eventually blocked constituted the 'noise-alone' recording. The
195 shaded regions that also extend across all panels of Figure 1 mark files that were selected for
196 subsequent minis' distribution fitting analyses. In this example files 27 to 88 and files 100 to 104
197 were selected for further analyses (10 recording sweeps per each file).

198

199 The remaining panels of Figure 1 were used to guide the data selection for subsequent analyses. The
200 standard deviation (SD) of the V_m (Figure 1B) was useful in determining the borders of different
201 recording types. Stable prolonged decreases in SD reliably indicated when APs or minis were
202 effectively blocked by corresponding pharmacological agents. Sudden brief increases in SD flagged
203 problematic recording segments containing higher levels of noise or V_m glitches. Gradual increases in
204 SD suggested the ensuing gradual deterioration of the recording quality.
205
206 Similar information was also provided by the evolution of amplitudes of the top 10% (amplitude-
207 wise) of all detected minis-like events in a single sweep (Figure 1C). Prolonged drop in the
208 amplitudes marked borders between recording types, while sudden jumps were indicative of V_m
209 instabilities. Finally, effective decay time constants of the same top 10% (amplitude-wise) of
210 detected events (Figure 1D) could be used as an indicator for the presence/absence of minis.
211 Blocking minis resulted in time constants becoming large indicating that only noise fluctuations were
212 being detected that did not possess typical decay dynamics common to PSPs.
213
214 Further insights into the recording quality over time were provided by impulse based measures.
215 Passive membrane time constant measurements over time (Figure 1E) were expected to remain
216 stable. Deviations from this expectation could signal a change in passive membrane properties and
217 the degradation in the recording quality. Total membrane capacitance (Figure 1F) was also expected
218 to be stable over time. Change in the capacitance could indicate tear of the membrane. Finally, input
219 resistance (the bridge balance error; Figure 1G) was not permitted to deviate by more than twice its
220 estimate obtained at the beginning of the recording. Violation of this rule of thumb indicated a
221 deterioration in the recording quality potentially resulting from debris accumulating in the recording
222 pipette or other reasons.
223

We obtained the above-discussed 7 longitudinal recording state/quality indicators for all our recordings. Multipaneled graphs showing these indicators for each individual recording separately are provided in Supplementary Figures 1-13.

Simulations

Simulating distributions of miniature excitatory postsynaptic potentials with a range of amplitudes and rise times

All simulations were carried out using 'minis' software developed in Matlab (Mathworks; RRID:SCR_001622) and performed on Cardiff School of Biosciences' Biocomputing Hub HPC/Cloud infrastructure. Simulation of minis-like events was based on an analytical solution to the passive cable equation for a transient current (Rall, 1977) using 100 lumped terms with a double exponential synaptic current with τ_1= 0.15-3 ms (optimised) and τ_2 = 2 ms (Major et al., 1993). The detailed description of how arbitrary shape PSPs were obtained is provided in our companion article (Dervinis and Major, 2023).

A pool of simulated events was generated combining 4 bivariate (amplitude and 10-90% rise time) normal distributions. 6 parameters described each distribution: amplitude mean μ_X and standard deviation σ_X, 10-90% rise time mean μ_Y and standard deviation σ_Y, a correlation factor ρ, and a scale factor n:

$$f(x,y) = \frac{n}{2\pi\sigma_X\sigma_Y\sqrt{1-\rho^2}} e^{-\frac{1}{2(1-\rho^2)}\left(\left(\frac{x-\mu_X}{\sigma_X}\right)^2 - 2\rho\left(\frac{x-\mu_X}{\sigma_X}\right)\left(\frac{y-\mu_Y}{\sigma_Y}\right) + \left(\frac{y-\mu_Y}{\sigma_Y}\right)^2\right)}.$$

All distribution parameters were controlled by the GA.

Fitting distributions of detected real minis-like events

Matlab's ga function was used to control 24 parameters describing 4 bivariate normal distributions (6 paprameters per distribution). Additional controlled parameters were the synaptic rise time

constant τ_1 which ranged between 0.15 and 3 ms and the passive membrane time constant τ_m. The range for the latter constant was taken to be between 0.95 times and 1.05 times the initial estimate based on the average waveform of all minis-like events detected in the 'noise + real minis' recording. Thus, there were 26 parameters in total controlled by the GA.

The GA would start by generating multiple distributions smEPSPs (i.e., 'individuals'; we used 260 individuals per 'generation'). Events would be drawn pseudo-randomly from a distribution and then simulated events of the right shape (in terms of amplitude and 10-90% rise time) would be superimposed on the 'noise-alone' recording at time points that were chosen pseudo-randomly (Figure 2). For generating the initial set of individuals ('population'), the GA chose parameters pseudo-randomly within prescribed ranges. For each of the four bivariate normal distributions the parameter ranges were as follows: μ_X (-0.1-1 mV), σ_X (0.01-1 mV), μ_Y (-2.5-10 ms), σ_Y (0.25-10 ms), ρ (-1 to 1), and n (0-10000 for the first distribution and –10000 to 10000 for the remaining three distributions). Any negative count bins within the resulting final distribution were zeroed out.

In the next step the GA assessed the fitness of each individual in the generation by using the cost function. The top 5% of the most fit individuals survived to the next generation without change while individual crossover, genetic migration, and other GA parameters were set to default values of the Matlab's ga function except for the mutation function type which was set to 'mutationadaptfeasible'. A new evolved generation of individuals was then created. Which then served as the basis for yet another generation. This process was repeated until an individual with the lowest cost (highest fitness value) possible was created, there was no improvement in the fitness for 100 consecutive generations, or the number of generations reached 1000.

In the case when the GA terminated without attaining the highest possible fitness value, distribution fitting procedure was reinitiated using the most fit individual as a seed. The population genetic

275 diversity was reset by setting the GA-controlled parameter ranges to ±5% of the original ranges
276 relative to the seed parameters. The rerunning of distribution fitting was repeated until the GA
277 generated the most fit individual possible, an acceptable level of fitness was reached (defined in the
278 next subsection), or there was no improvement in fitness compared to the previous run.
279
280 If the most fit individual was within acceptable levels of fitness values, the lower threshold on
281 smEPSP amplitude was increased by 0.005 mV and the entire fitting procedure rerun from the
282 beginning till the end. This procedure was repeated until the GA stopped converging on a solution
283 with acceptable fitness values. The reason for pushing the lower limit of smEPSPs' amplitudes is that
284 GA-generated solutions are not unique. Matching 'noise + real minis' recording can be achieved by
285 using a distribution of fewer relatively large amplitude smEPSPs or more numerous smaller
286 amplitude smEPSPs. There is an infinite number of such distributions with ever decreasing
287 amplitudes of smEPSPs. Therefore, GA has no guaranteed way of arriving at the proven true
288 distribution of minis, only at an upper amplitude limit of this distribution by the above-described
289 thresholding procedure.
290
291 *Cost function*
292 The goal of the minis' distribution fitting procedure was to match 'noise + simulated minis' and
293 'noise + real minis' recordings as close as possible in terms of the distribution of amplitudes and 10-
294 90% rise times of detected minis-like events in the two types of V_m recording traces ('simulated' vs
295 'real' distributions). This was achieved by minimising the cost function using the GA. The cost
296 function was composed of three types of components: shape constraints on the simulated minis
297 distribution, sums of absolute deviations (SADs) between 'simulated' and 'real' distributions, and
298 maximal absolute deviations (MADs) between 'simulated' and 'real' distributions.
299

We calculated the typical ranges of SADs and MADs for each of the 14 recordings by taking the individual 'noise + real minis' recording and dividing it into smaller files typically consisting of 5 sweeps each (to match the size of the segment of 'noise-alone' recording used in the distribution fitting procedure). Each file in this set was subjected to minis detection procedure resulting in a set of 'real' distributions. They were then subtracted from each other, and corresponding SAD and MAD scores were calculated for each possible n*(n-1) file combinations. 6 different SAD and MAD scores were calculated based on: distributions of (1) amplitudes of all detected events, (2) amplitudes of top 50% largest detected events, (3) amplitudes of top 10% largest detected events, (4) amplitudes of top 2% largest detected events, (5) distribution of 10-90% rise times, and (6) a joint amplitude and 10-90% rise time distribution. The smallest percentile that guaranteed to include half of SAD or MAD scores of all file combinations simultaneously for all 6 types of scores ('6-score combined 50th centile') was used to determine which SAD or MAD values should be used for all 6 types of scores to construct the cost function.

The cost function was constructed of 6 types of SAD scores and 6 types of MAD scores estimated using the '6-score combined 50th centile' procedure. Additional 3 SAD scores were added to penalise 'simulated' amplitude distributions that had lower counts of high amplitude events (top 50%, 10%, and 2%) compared to 'real' distributions. These 15 scores were used to evaluate how close the 'simulated' distribution was to a single selected 'real' distribution that was deemed to be of the best quality by a human observer. Additional corresponding 15 'deviation' scores (same as SADs and MADs but comparing to all distributions at once) were calculated assessing how much each 'real' or 'simulated' distribution deviated from the full set consisting of all 'real' distributions and the single 'simulated' distribution. The 'simulated' distribution was expected to have a lower deviation score than the worst performing 'real' distribution. 'Simulated' distributions were further penalised if their underlying 'simulated minis' distribution violated the 10-90% rise time skewness constraint which stipulated that the mean 10-90% rise time of simulated minis should exceed the median. Finally,

326 ‘simulated’ distributions were also penalised if their underlying ‘simulated minis’ amplitude
327 distribution had a sharp cliff at its lower end. Hence, there were 32 fitness components in total (15 +
328 15 + 1 + 1 = 32).
329
330 If all amplitude SAD, MAD, and deviation scores for comparing the ‘simulated’ distribution to the
331 closest ‘real’ distribution were satisfied at the end of the fitting procedure, the fit was deemed to be
332 ‘good enough’. Alternatively, the fit could also be deemed good enough if all amplitude and 10-90%
333 rise time SAD and MAD scores were satisfied (deviation scores excluded).
334
335 **Statistical analyses**
336 All inferential statistics were based on the assumption that distributions of all measures were
337 normal. All mean distribution values are stated/depicted with 95% confidence limits.
338
339 **Data accessibility**
340 All data analysed in this study are publicly available (GIN DOI will appear in version 2 of the
341 manuscript). The available data include ‘noise + minis’ and ‘noise-alone’ whole-cell patch membrane
342 potential recordings that were used in computer simulations and minis’ distribution fitting. All
343 electrophysiological recordings were stored in Axon Binary File (ABF) format.
344
345 **Code accessibility**
346 All analyses were carried out in Matlab and the analysis code is publicly available on GitHub (DOI will
347 appear in version 2 of the manuscript). The code is complete with instructions on how to reproduce
348 all figures reported in this study.
349
350 **Software accessibility**

351 The present study reported the use of a novel quantal analysis method that is part of 'minis'
352 software available on GitHub (Dervinis, 2022).
353

354 Results

355 *Estimating quantal size by direct subtraction of noise component*
356 We have subjected 'noise + minis' recordings and 'noise-alone' recordings to the 'minis' detection
357 algorithm. Detected mEPSP-like events had a particular shape amplitude and 10-90% rise time
358 distributions that resembled log-normal or gamma distributions (Figure 3). In the amplitude domain
359 the lower end of the distribution contains a mixture of real minis and noise fluctuations that were
360 misidentified as real events.
361
362 We argued that if the noise component could be reliably estimated based on the 'noise-alone'
363 recording where synaptic activity has been pharmacologically blocked, it could be directly subtracted
364 from the 'noise + minis' distribution yielding an estimate of the pure minis' component. Figure 3A
365 shows both 'noise + minis' and 'noise-alone' detected event amplitude distributions superimposed
366 over each other. After subtracting the 'noise-alone' distribution from the 'noise + minis' distribution
367 there appear negative low amplitude bins in the resulting distribution (indicated by an arrowhead in
368 Figure 3A). These missing low amplitude events are caused by larger minis overshadowing smaller
369 minis and noise fluctuations in the 'noise + minis' recording (we have discussed this phenomenon in
370 great length in our companion article (Dervinis and Major, 2023)). Therefore, the direct subtraction
371 approach can only provide a high-end upper limit on the mean of the minis' amplitude distribution.
372
373 Nevertheless, this over-estimate is more reliable than a highly subjective approach of simply
374 estimating the mean amplitude based on events detected using a high amplitude threshold. Figure 4
375 shows the distribution of mean minis' amplitudes obtained using the direct noise subtraction

376 method. When mean amplitude estimates are compared to capacitance estimates (or
377 1/capacitance), there is a strong inverse correlation between the mean amplitude and cell's
378 capacitance (the proxy measure for cell's size; $r = 0.754$, $p = 0.00275$, $R^2 = 0.568$). That is, the larger
379 the cell, the smaller the amplitude of its somatically detected minis and vice-versa. This relationship
380 is predicted by the theory of capacitors ($C = Q/V$, where C stands for capacitance, Q stands for
381 charge, and V stands for voltage across the cell's membrane), and it is a direct demonstration
382 attenuating effect of cell's capacitance on the amplitude of somatically detected minis. If a direct
383 line was drawn through the data and the origin of the axes in Figure 4, the slope of this line would
384 provide a quantal size estimate for excitatory synapses in the CNS in terms of charge ($Q = \Delta V/$
385 $\Delta(1/C)$) which is approximately equal to 34.33 fC in this case.
386
387 *Estimating quantal size by simulating excitatory postsynaptic potential source distribution*
388 An alternative and more reliable way of estimating the quantal size in our recordings is to estimate
389 the minis component directly using simulations. This relies on 'minis' optimisation algorithm (GA)
390 being able to closely match a 'noise + simulated minis' voltage trace (Figure 2) with 'noise + real
391 minis' recordings in terms of amplitude and 10-90% rise time distributions of minis-like events
392 detected within these traces. We were able to successfully do that for all our recordings (see Figure
393 5 and Supplementary Figures 14-26) with one particular example shown in Figure 5. All simulations
394 produced 'good enough' matches showing amplitude and 10-90% rise time distributions of detected
395 minis-like events being within the range of amplitude and 10-90% rise time count values measured
396 in sets of 'real event' distributions. All resulting minis source distributions are displayed in Figure 6
397 and Supplementary Figures 27-39. An example in Figure 6 shows that the 'real minis' source
398 distribution likely has a log-normal or gamma-like shape in both amplitude and rise time domains.
399
400 Incidence rates estimated based on simulated minis source distributions ranged roughly between 10
401 and 100 minis/s (Figure 7). This is estimate is an order of magnitude higher than the one based on

402 the literature and significantly higher than the one based on the direct subtraction method (t(13) =
403 4.33, p = 0.0008) and also higher than the estimate based on amplitudes higher than a chosen 0.8
404 mV threshold (t(13) = 4.89, p = 0.0003). It is precisely within the range predicted in our companion
405 article (Dervinis and Major, 2023). However, this range is still somewhat of an underestimate as
406 minis source distributions were often generated using a lower limit on simulated amplitudes to
407 constrain the distribution non-uniqueness as discussed in the methods subsection on the
408 distribution fitting.
409
410 Mean minis' amplitudes derived using simulations ranged between 0.053 and 0.14 mV (Figure 8A).
411 Just like amplitudes derived by the noise subtraction method in Figure 4, amplitudes derived using
412 simulations had a strong association with the size of the cell represented by cell's capacitance
413 (Figure 8A). The effect size of this relationship was even stronger for simulated amplitudes
414 explaining 63% of the total variance (r = 0.793, p = 0.00115). The slope of the line fitted through the
415 data and passing the origin of axes in Figure 8A provided the estimate of quantal size in the cortical
416 excitatory synapses that was approximately equal to 28.53 fC and, as expected, was smaller than
417 that derived by the noise subtraction method. The two types of mean amplitude estimates derived
418 either by noise subtraction or by minis source distribution simulation were mutually correlated (r =
419 0.596, p = 0.0275, R^2 = 0.355, Figure 8B). The equation of the line (1.01x + 0.005) fitted to this data
420 provided a way to approximate the mean amplitude of fitted minis' source distribution by adding the
421 intercept term to the means derived by noise subtraction (no multiplication term as the slope of the
422 line was approximately equal to 1).
423
424 *Generic miniature excitatory postsynaptic potential distribution in neocortex*
425 To construct a generic mEPSP distribution, we normalised amplitudes of simulated minis' source
426 distributions shown in Figure 6 and Supplementary Figures 27-39 by dividing them by their
427 respective means and taking the total average. The resulting combined (amplitude and 10-90% rise

time) distribution is shown in Figure 9A and its smoothed version is shown in Figure 9B. The corresponding marginal amplitude and 10-90% rise time distributions are shown in Figures 9C and E, respectively, with their smoothed versions shown in Figures 9D and F. Both marginal distributions have a log-normal or gamma-like distributions.

Discussion

In this article we reported two major scientific advances. First, we described a novel quantal analysis method that is based on separate somatic recordings of mEPSPs in the background of physiological noise and recordings of noise alone after pharmacological blockade of mEPSPs. The latter type of recording provides a means to estimate the properties of the noise component which can then be used to account for noise fluctuations in the combined minis and noise recording. However, this was done not by a direct subtraction of the noise component but rather by the simulation of the underlying minis component and repeatedly superimposing simulated minis shapes onto the noise trace until the 'noise + simulated minis' voltage trace closely matched the 'noise + real minis' recording. The key tool to achieving this match was the GA that optimised the parameters of the simulated minis distribution in terms of amplitudes and 10-90% rise times.

The second major advance was the use case for the novel quantal analysis method that successfully measured the electrical size of excitatory synapses of cortical pyramidal cells which was shown to be approximately equal to 28.53 fC. This number was inferred from the slope of the line fitting minis' mean amplitude and cell's total capacitance data in accordance with the theory of capacitors. The fact that this line had an intercept at the origin of the axes indicated that there was no active compensation for minis' amplitude attenuation due to cell's size (i.e., total capacitance). Indeed, cell's capacitance played a major role affecting the amplitude of mEPSPs resulting in a large proportion of mEPSPs being otherwise indistinguishable from noise. The number of these so-called

453 ‘missing’ minis was so high that the estimated minis’ incidence rate was in the order of 10-100
454 minis/s: A number that is larger by an order of magnitude than the one typically encountered in the
455 synaptic physiology literature. Finally, both the amplitude and 10-90% rise time distributions of minis
456 had a log-normal- or gamma-like shapes.
457
458 These findings have a few major implications. First, the method, as used for estimating the mEPSPs’
459 distributions in cortical layers 2/3 and 5 of cells of various size and then using these distributions to
460 arrive at the electrical size of excitatory synapses serves as a proof of principle that it can be
461 successfully used to estimate PSP distributions of various types in the CNS. The next logical step of
462 this method is to extend its application to the estimation of amplitude and rise time distributions of
463 mIPSPs generated by different types of inhibitory synapses and, as a result, the electrical sizes of
464 these different inhibitory synapses. Moreover, the ability to get relatively accurate quantal size
465 estimates unobscured by physiological noise is important for constraining synaptic parameters in
466 physiologically realistic simulations of neural activity. For example, now we should be able to
467 estimate how many active synapses are needed to generate an NMDA spike within a single dendritic
468 segment (Major et al., 2013b). The importance of these number estimates is not restricted to the
469 domain of physiologically realistic simulations but also extends to more abstract computations that
470 use NMDA spike-like mechanisms as coincidence detectors in latest cortically inspired models of
471 artificial intelligence (Hawkins et al., 2019). It is thus imperative to arrive at accurate estimates of
472 synaptic transmission parameters.
473
474 These findings also draw attention to methodological issues in the field of synaptic physiology. As
475 discussed in our companion article (Dervinis and Major, 2023), the commonly reported incidence
476 rates for mEPSCs are well below 10 minis/s. Even if one is in doubt of the incidence rates that we
477 arrived with the help of simulations that lie in the range of 10-100 minis/s, the range of incidence
478 rates given by direct subtraction of the distribution of events detected in the ‘noise-alone’ recording

479 from the distribution based on the 'noise + minis' recording is still within 5.9 and 26.7 minis/s which
480 we know to be an underestimate. Therefore, reported minis' incidence rates below 10 minis/s are
481 certainly underestimates. As discussed earlier, these estimates could be improved by switching to
482 voltage recording instead of using the voltage clamp (Major, 1993; Rall and Segev, 1985; Spruston et
483 al., 1993; Williams and Mitchell, 2008). But more importantly, a strong association between cell's
484 capacitance (or its size) and how much somatically recorded minis' amplitudes are attenuated
485 indicates that special care must be taken to account for the effect of background noise fluctuations
486 on the amplitude measurements as we have done here. This association is yet another evidence
487 supporting experimental observations of massive minis' amplitude attenuation as the PSP spreads
488 from its dendritic source location to the soma (Larkum et al., 2009; Major et al., 2013a; Nevian et al.,
489 2007; Stuart and Spruston, 1998; Williams and Mitchell, 2008; Williams and Stuart, 2002).
490
491 It is also important to note that understanding the link between cell's capacitance and somatically
492 recorded minis' average amplitudes as well as knowing actual shapes of minis' distributions in terms
493 of their amplitudes and rise times allows us to generate artificial data where ground truth data is
494 known. Such labelled data could be used to train artificial neural networks (ANNs) which could then
495 be used develop the next generation powerful quantal analysis methods allowing detection of minis
496 directly in mixed 'noise + minis' recordings. Such methods would not only do away with the need to
497 obtain relatively long voltage recordings with consecutive pharmacological phases but could
498 potentially fully automate the minis' detection process. We are not the first to suggest the
499 application of ANNs to this issue (see (Pircher et al., 2022) and (Wang et al., 2024)). However, we are
500 not aware of attempts to use realistic minis' distributions for this purpose.
501
502 Even though the novel quantal analysis method we present here is an important advancement, it
503 nevertheless has limitations. One of them is the need for long duration recordings using different
504 pharmacological agents at various stages of recording. However, the somatic recording set up is not

505 as complicated as an alternative multisite dendritic recording set up would be. Moreover, the
506 distribution fitting procedure involving the GA can be lengthy and computationally intensive.
507 However, 'minis' software is parallelised at the PSP detection level, as well as at the GA optimisation
508 level making it particularly suitable to be executed on multi-core computing cluster. Although 'minis'
509 software combined with the two-stage recording set up offers an unprecedented control potential
510 over the background physiological noise, we understand that many researchers may not be
511 persuaded to adopt it themselves. Therefore, the adoption of ANNs for the next generation of
512 'minis' software based on current findings and future use-cases offers a way to simplify the current
513 approach.
514
515 Some researchers may be critical of a method that does not rely on a direct measurement of minis
516 but rather on an approximation via indirect means using simulations. This is a valid criticism that
517 could be addressed in the future by using a method of repeatedly subjecting a voltage recording to
518 minis detection procedure with increasingly lower threshold while subtracting detected events from
519 the voltage recording. This approach potentially could recover most of the smaller minis that are
520 overshadowed by the larger ones (the so called 'negative bins' problem illustrated in Figure 3A).
521 Furthermore, other researchers may question the ability to pharmacologically isolate the
522 background physiological noise. Our 'noise-alone' recordings may contain random openings of
523 individual AMPA channels or may fail to fully eliminate channel openings in the presence of quantal
524 release of neurotransmitter. Physiological noise itself may be different in the two conditions with
525 the presence or absence of mEPSP pharmacological blockers. Although there may be some reason to
526 suspect that may be the case, these factors are unlikely to have affected the results significantly due
527 to small amplitude nature of these membrane potential variations.
528

References

Bekkers JM. 1994. Quantal analysis of synaptic transmission in the central nervous system. *Curr Opin Neurobiol* **4**:360–365. doi:https://doi.org/10.1016/0959-4388(94)90097-3

Biró ÁA, Holderith NB, Nusser Z. 2005. Quantal Size Is Independent of the Release Probability at Hippocampal Excitatory Synapses. *The Journal of Neuroscience* **25**:223–232. doi:10.1523/JNEUROSCI.3688-04.2005

Brown TH, Wong RKS, Prince DA. 1979. Spontaneous miniature synaptic potentials in hippocampal neurons. *Brain Res* **177**:194–199. doi:https://doi.org/10.1016/0006-8993(79)90931-4

Clamann HP, Rioult-Pedotti MS, Luscher HR. 1991. The influence of noise on quantal EPSP size obtained by deconvolution in spinal motoneurons in the cat. *J Neurophysiol* **65**:67–75. doi:10.1152/jn.1991.65.1.67

Clements JD. 2003. Variance–mean analysis: a simple and reliable approach for investigating synaptic transmission and modulation. *J Neurosci Methods* **130**:115–125. doi:https://doi.org/10.1016/j.jneumeth.2003.09.019

Clements JD, Silver RA. 2000. Unveiling synaptic plasticity: a new graphical and analytical approach. *Trends Neurosci* **23**:105–113. doi:10.1016/S0166-2236(99)01520-9

del Castillo J, Katz B. 1954. Quantal components of the end-plate potential. *J Physiol* **124**:560–573. doi:https://doi.org/10.1113/jphysiol.1954.sp005129

Dervinis M, Major G. 2023. A novel method for reliably measuring miniature and spontaneous postsynaptic potentials/currents in whole-cell patch clamp recordings in the central nervous system. *bioRxiv*. doi:10.1101/2022.03.20.485046

Edwards FR, Redman SJ, Walmsley B. 1976. Statistical fluctuations in charge transfer at Ia synapses on spinal motoneurones. *J Physiol* **259**:665–688. doi:https://doi.org/10.1113/jphysiol.1976.sp011488

553 Enoki R, Hu Y, Hamilton D, Fine A. 2009. Expression of Long-Term Plasticity at Individual Synapses in
554 Hippocampus Is Graded, Bidirectional, and Mainly Presynaptic: Optical Quantal Analysis.
555 *Neuron* **62**:242–253. doi:10.1016/j.neuron.2009.02.026
556 Fatt P, Katz B. 1952. Spontaneous subthreshold activity at motor nerve endings. *J Physiol* **117**:109–
557 128.
558 Forti L, Bossi M, Bergamaschi A, Villa A, Malgaroli A. 1997. Loose-patch recordings of single quanta at
559 individual hippocampal synapses. *Nature* **388**:874–878. doi:10.1038/42251
560 Hardingham NR, Read JCA, Trevelyan AJ, Nelson JC, Jack JJB, Bannister NJ. 2010. Quantal Analysis
561 Reveals a Functional Correlation between Presynaptic and Postsynaptic Efficacy in Excitatory
562 Connections from Rat Neocortex. *The Journal of Neuroscience* **30**:1441–1451.
563 doi:10.1523/JNEUROSCI.3244-09.2010
564 Hawkins J, Lewis M, Klukas M, Purdy S, Ahmad S. 2019. A Framework for Intelligence and Cortical
565 Function Based on Grid Cells in the Neocortex. *Front Neural Circuits* **12**.
566 doi:10.3389/fncir.2018.00121
567 Heuser JE, Reese TS, Dennis MJ, Jan Y, Jan L, Evans L. 1979. Synaptic vesicle exocytosis captured by
568 quick freezing and correlated with quantal transmitter release. *Journal of Cell Biology* **81**:275–
569 300. doi:10.1083/jcb.81.2.275
570 Isaacson JS, Walmsley B. 1995. Counting quanta: Direct measurements of transmitter release at a
571 central synapse. *Neuron* **15**:875–884. doi:10.1016/0896-6273(95)90178-7
572 Jack JJ, Redman SJ, Wong K. 1981. The components of synaptic potentials evoked in cat spinal
573 motoneurones by impulses in single group Ia afferents. *J Physiol* **321**:65–96.
574 doi:https://doi.org/10.1113/jphysiol.1981.sp013972
575 Jonas P, Major G, Sakmann B. 1993. Quantal components of unitary EPSCs at the mossy fibre
576 synapse on CA3 pyramidal cells of rat hippocampus. *J Physiol* **472**:615–663.
577 doi:https://doi.org/10.1113/jphysiol.1993.sp019965
578 Katz B. 1969. The Release of Neural Transmitter Substances. Liverpool: Liverpool Univ. Press.

579 Korn H, Faber DS. 1991. Quantal analysis and synaptic efficacy in the CNS. *Trends Neurosci* **14**:439–
580 445. doi:https://doi.org/10.1016/0166-2236(91)90042-S
581 Kraszewski K, Grantyn R. 1992. Unitary, quantal and miniature gaba-activated synaptic chloride
582 currents in cultured neurons from the rat superior colliculus. *Neuroscience* **47**:555–570.
583 doi:https://doi.org/10.1016/0306-4522(92)90165-X
584 Kullmann DM, Nicoll RA. 1992. Long-term potentiation is associated with increases in quantal
585 content and quantal amplitude. *Nature* **357**:240–244. doi:10.1038/357240a0
586 Kuno M. 1964. Quantal components of excitatory synaptic potentials in spinal motoneurones. *J*
587 *Physiol* **175**:81–99. doi:https://doi.org/10.1113/jphysiol.1964.sp007504
588 Larkman A, Stratford K, Jack J. 1991. Quantal analysis of excitatory synaptic action and depression in
589 hippocampal slices. *Nature* **350**:344–347. doi:10.1038/350344a0
590 Larkum ME, Nevian T, Sandler M, Polsky A, Schiller J. 2009. Synaptic Integration in Tuft Dendrites of
591 Layer 5 Pyramidal Neurons: A New Unifying Principle. *Science (1979)* **325**:756–760.
592 doi:10.1126/science.1171958
593 Liu Z, Lu X, Villette V, Gou Y, Colbert KL, Lai S, Guan S, Land MA, Lee J, Assefa T, Zollinger DR,
594 Korympidou MM, Vlasits AL, Pang MM, Su S, Cai C, Froudarakis E, Zhou N, Patel SS, Smith CL,
595 Ayon A, Bizouard P, Bradley J, Franke K, Clandinin TR, Giovannucci A, Tolias AS, Reimer J,
596 Dieudonné S, St-Pierre F. 2022. Sustained deep-tissue voltage recording using a fast indicator
597 evolved for two-photon microscopy. *Cell* **185**:3408-3425.e29. doi:10.1016/J.CELL.2022.07.013
598 Major G. 1993. Solutions for transients in arbitrarily branching cables: III. Voltage clamp problems.
599 *Biophys J* **65**:469–491. doi:10.1016/S0006-3495(93)81039-7
600 Major G, Evans J D, Jack J J. 1993. Solutions for transients in arbitrarily branching cables: I. Voltage
601 recording with a somatic shunt. *Biophys J* **65**:423–449.
602 Major G, Evans JD, Jack JJ. 1993. Solutions for transients in arbitrarily branching cables: I. Voltage
603 recording with a somatic shunt. *Biophys J* **65**:423–449. doi:10.1016/S0006-3495(93)81037-3

Major G, Larkum ME, Schiller J. 2013a. Active Properties of Neocortical Pyramidal Neuron Dendrites. *Annu Rev Neurosci* **36**:1–24. doi:10.1146/annurev-neuro-062111-150343

Major G, Larkum ME, Schiller J. 2013b. Active Properties of Neocortical Pyramidal Neuron Dendrites. *Annu Rev Neurosci* **36**:1–24. doi:10.1146/annurev-neuro-062111-150343

Nevian T, Larkum ME, Polsky A, Schiller J. 2007. Properties of basal dendrites of layer 5 pyramidal neurons: a direct patch-clamp recording study. *Nat Neurosci* **10**:206–214. doi:10.1038/nn1826

Oertner TG, Sabatini BL, Nimchinsky EA, Svoboda K. 2002. Facilitation at single synapses probed with optical quantal analysis. *Nat Neurosci* **5**:657–664. doi:10.1038/nn867

Peled ES, Isacoff EY. 2011. Optical quantal analysis of synaptic transmission in wild-type and rab3-mutant Drosophila motor axons. *Nat Neurosci* **14**:519–526. doi:10.1038/nn.2767

Pircher T, Pircher B, Feigenspan A. 2022. A novel machine learning-based approach for the detection and analysis of spontaneous synaptic currents. *PLoS One* **17**:1–16. doi:10.1371/journal.pone.0273501

Rall W. 1977. Core Conductor Theory and Cable Properties of Neurons In: Kandel ER, Brookhardt JM, Mountcastle VM, editors. Handbook of Physiology, Cellular Biology of Neurons. Bethesda, MD: American Physiological Society. pp. 39–97.

Rall W, Segev I. 1985. Space-clamp problems when voltage clamping branched neurons with intracellular microelectrodes In: T. G. Smith Jr, Lecar H, Redman SJ, Gage P, editors. Voltage and Patch Clamping with Microelectrodes. Bethesda, MD: American Physiological Society. pp. 191–215.

Redman S. 1990. Quantal analysis of synaptic potentials in neurons of the central nervous system. *Physiol Rev* **70**:165–198. doi:10.1152/physrev.1990.70.1.165

Reid CA, Clements JD. 1999. Postsynaptic expression of long-term potentiation in the rat dentate gyrus demonstrated by variance-mean analysis. *J Physiol* **518**:121–130. doi:https://doi.org/10.1111/j.1469-7793.1999.0121r.x

Sahara Y, Takahashi T. 2001. Quantal components of the excitatory postsynaptic currents at a rat central auditory synapse. *J Physiol* **536**:189–197. doi:https://doi.org/10.1111/j.1469-7793.2001.00189.x

Silver RA. 2003. Estimation of nonuniform quantal parameters with multiple-probability fluctuation analysis: theory, application and limitations. *J Neurosci Methods* **130**:127–141. doi:https://doi.org/10.1016/j.jneumeth.2003.09.030

Spruston N, Jaffe DB, Williams SH, Johnston D. 1993. Voltage- and space-clamp errors associated with the measurement of electrotonically remote synaptic events. *J Neurophysiol* **70**:781–802. doi:10.1152/jn.1993.70.2.781

Stern P, Edwards FA, Sakmann B. 1992. Fast and slow components of unitary EPSCs on stellate cells elicited by focal stimulation in slices of rat visual cortex. *J Physiol* **449**:247–278. doi:https://doi.org/10.1113/jphysiol.1992.sp019085

Stuart G, Spruston N. 1998. Determinants of Voltage Attenuation in Neocortical Pyramidal Neuron Dendrites. *The Journal of Neuroscience* **18**:3501–3510. doi:10.1523/JNEUROSCI.18-10-03501.1998

Vere-Jones D. 1966. SIMPLE STOCHASTIC MODELS FOR THE RELEASE OF QUANTA OF TRANSMITTER FROM A NERVE TERMINAL. *Australian Journal of Statistics* **8**:53–63. doi:https://doi.org/10.1111/j.1467-842X.1966.tb00164.x

Wall MJ, Usowicz MM. 1998. Development of the quantal properties of evoked and spontaneous synaptic currents at a brain synapse. *Nat Neurosci* **1**:675–682. doi:10.1038/3677

Wang N-S, Marino M, Malinow R. 2024. Detecting unitary synaptic events with machine learning. *Proceedings of the National Academy of Sciences* **121**:e2315804121. doi:10.1073/pnas.2315804121

Williams SR, Mitchell SJ. 2008. Direct measurement of somatic voltage clamp errors in central neurons. *Nat Neurosci* **11**:790–798. doi:10.1038/nn.2137

654 Williams SR, Stuart GJ. 2002. Dependence of EPSP Efficacy on Synapse Location in Neocortical
655 Pyramidal Neurons. *Science (1979)* **295**:1907–1910. doi:10.1126/science.1067903
656 Yuste R, Majewska A, Cash SS, Denk W. 1999. Mechanisms of Calcium Influx into Hippocampal
657 Spines: Heterogeneity among Spines, Coincidence Detection by NMDA Receptors, and Optical
658 Quantal Analysis. *The Journal of Neuroscience* **19**:1976–1987. doi:10.1523/JNEUROSCI.19-06-
659 01976.1999
660
661

Figures

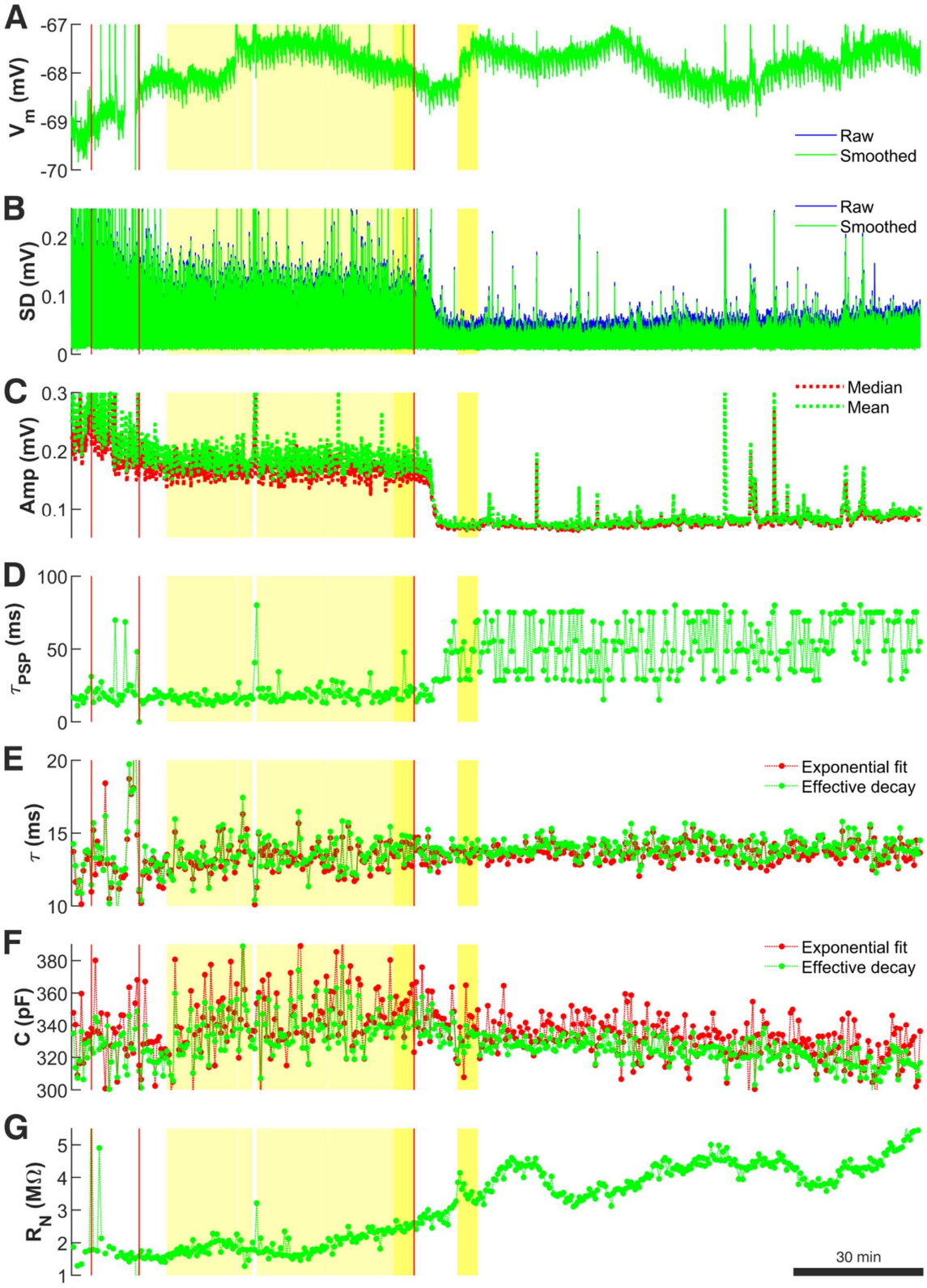

Figure 1: Recording quality measures used during the data preprocessing stage to select 'noise + minis' and 'noise-alone' recording sweeps for further data analysis for recording p103a (layer 5).

666 (A) Baseline V_m across the entire recording session. The raw trace is very similar to the smoothed
667 one and, therefore, is occluded by the latter. Stimulation pulses were excluded from the display. The
668 total recording duration (excluding pulse periods) was 8520 s. The first red vertical line marks the
669 time when pharmacological blockade of APs was initiated. The second red vertical line marks the
670 time when no more APs were observing in the recording. The third red vertical line marks the time
671 when pharmacological blockade of mEPSPs was initiated. Bright yellow periods mark 'noise + minis'
672 recording segment selected as the main comparison file for the distribution fitting. Light yellow
673 marks all the remaining good quality 'noise + minis' recording sweeps that were also included in the
674 distribution fitting procedure for estimating target SAD, MAD, and 'deviation' scores.
675 (B) V_m standard deviation measured over consecutive 15 ms windows over the same recording
676 session. The meaning of symbols is the same as in panel (A).
677 (C) Evolution of mean and median amplitudes of the top 10% (amplitude-wise) of all detected minis-
678 like events averaged over single sweeps across the entire recording session.
679 (D) Effective decay (drop to 1/e of the peak value) time constants of the same top 10% (amplitude-
680 wise) of detected events as in panel (C) averaged over consecutive 20-second-long segments across
681 the same session.
682 (E) Evolution of passive membrane time constant over the entire recording session. Measurements
683 were averaged over consecutive 20-second-long segments. Both measurements based on
684 exponential decay curve fit and on effective V_m drop to 1/e of the initial value were calculated and
685 displayed.
686 (F) Evolution of total cell's membrane capacitance across the recording session. Measurements were
687 averaged over consecutive 20-second-long segments. Both measurements based on exponential
688 decay curve fit and on effective V_m drop to 1/e of the initial value were calculated and displayed.
689 (G) Evolution of cell's input resistance (the bridge balance error) across the recording session.
690 Measurements were averaged over consecutive 20-second-long segments.

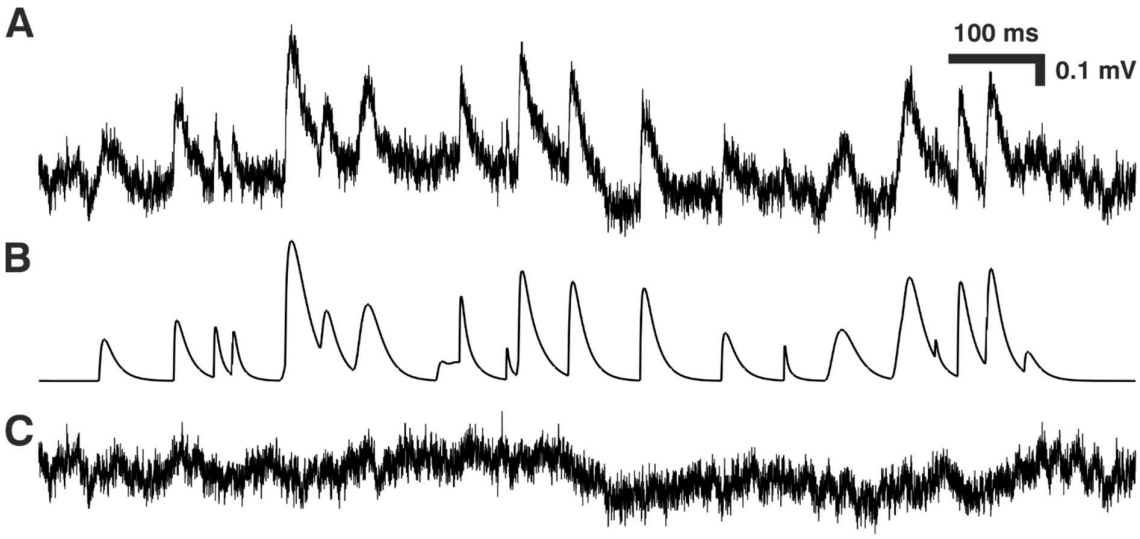

Figure 2: Constructing ’noise + simulated minis’ voltage trace.

(A) A voltage trace of a physiological noise recording superimposed with simulated mEPSPs.

(B) A voltage trace showing simulated mEPSPs only that were used to produce the voltage trace in (A).

(C) A segment of ‘noise-alone’ recording that was used to produce the voltage trace in (A). The noise recording was obtained from cell p131a in the cortical layer 2/3.

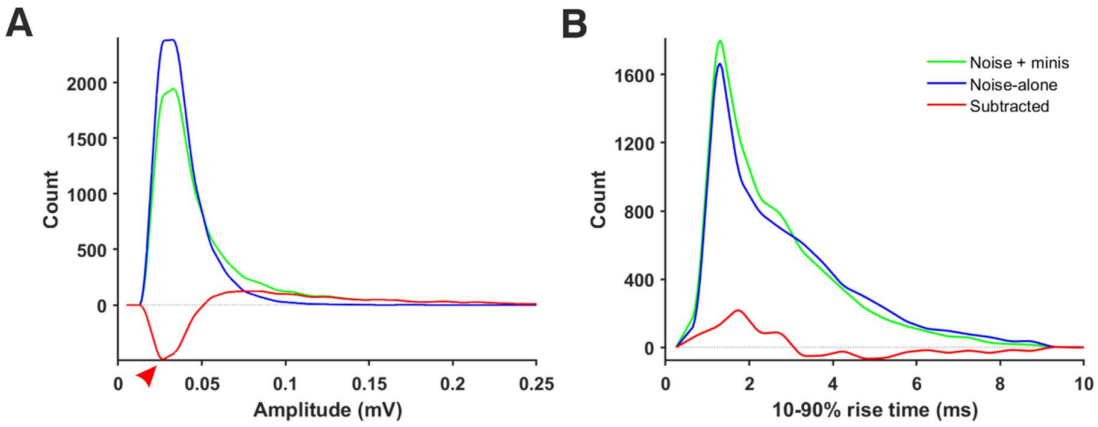

Figure 3: Amplitude and rise time distributions of detected minis-like events in ’noise + minis’ and ’noise-alone’ recordings.

(A) Amplitude distributions of detected minis-like events in ’noise + minis’ and ’noise-alone’ recordings (p108b cell in the cortical layer 5). The legend is provided in panel (B). The read arrowhead indicates negative bins after subtracting ‘noise-alone’ distribution from ‘noise + minis’ distribution.

(B) 10-90% rise time distributions of detected minis-like events in ’noise + minis’ and ’noise-alone’ recordings.

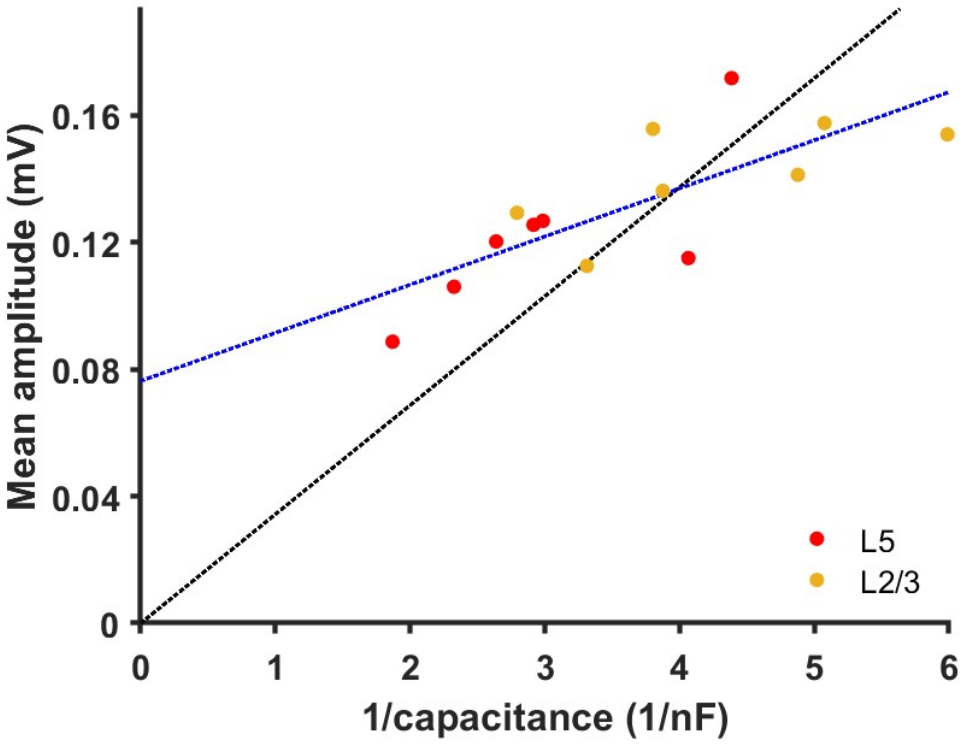

Figure 4: Relationship between the inverse of cell's total capacitance and the mean amplitude of minis recorded at its soma after subtracting the amplitude distribution based on the 'noise-alone' recording from the amplitude distribution based on the 'minis + noise' distribution. The blue line is the least square fit to the data while the black line is the fit to the data that passes through the origin of the axes.

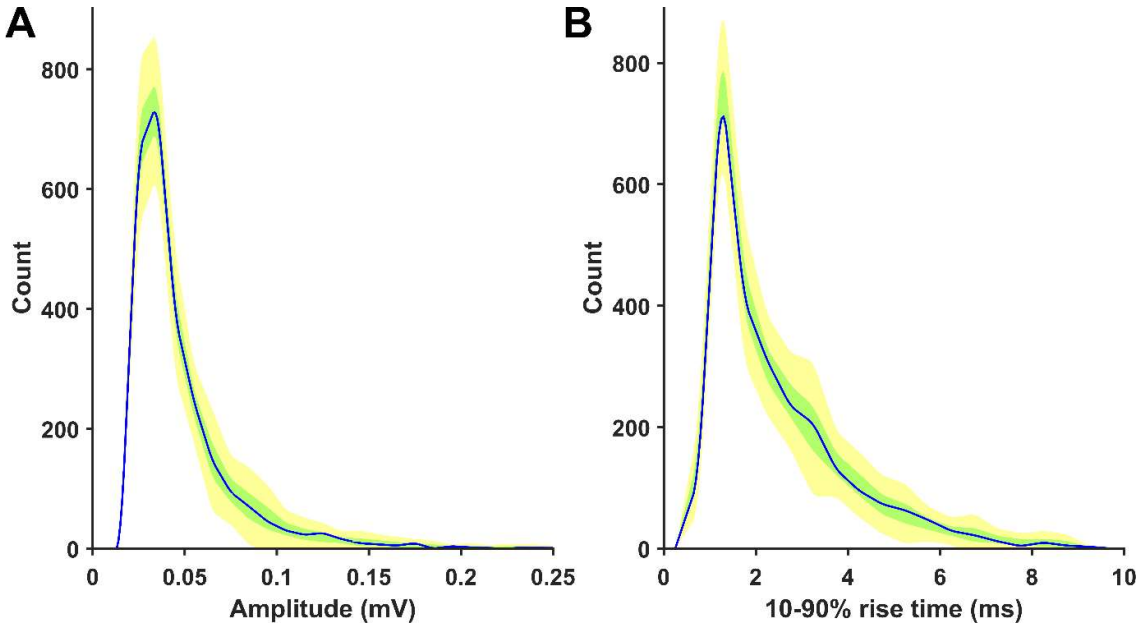

Figure 5: Distributions of minis-like events detected in a ’noise + simulated minis’ voltage trace that closely matched ‘noise + real minis‘ recordings.

Parameters of simulated minis were controlled by the GA, whereas the ’noise-alone’ recording was obtained in cell p106b of the cortical layer 5. Interval marked by green indicates the range of values across multiple ‘noise + real minis’ recording files. The yellow shaded interval indicates the triple size range.

(A) Amplitude distribution of minis-like events detected in a ’noise + simulated minis’ voltage trace (the blue curve).

(B) 10-90% rise time distribution of minis-like events detected in a ’noise + simulated minis’ voltage trace (the blue curve).

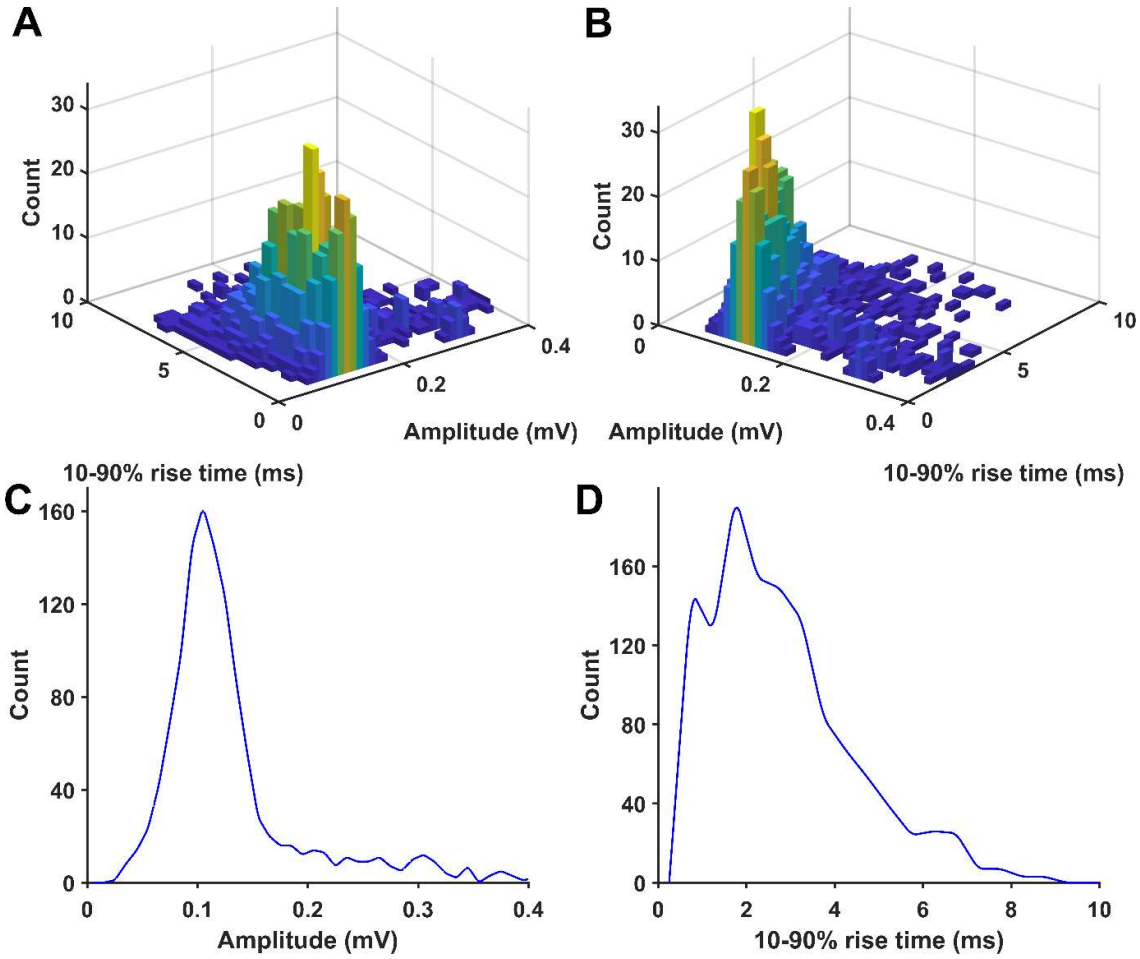

Figure 6: An example of simulated minis distribution that was used to produce a close match between distributions of detected minis-like events in a ’noise + simulated minis’ voltage trace and in a ’noise + real minis’ recording for a cell p131c of cortical layer 2/3.

(A) A joint amplitude and 10-90% rise time distribution of simulated minis.

(B) The same distribution but viewed from a different angle.

(C) Marginal amplitude distribution of the same distribution as in (A).

(D) Marginal 10-90% rise time distribution of the same distribution as in (A).

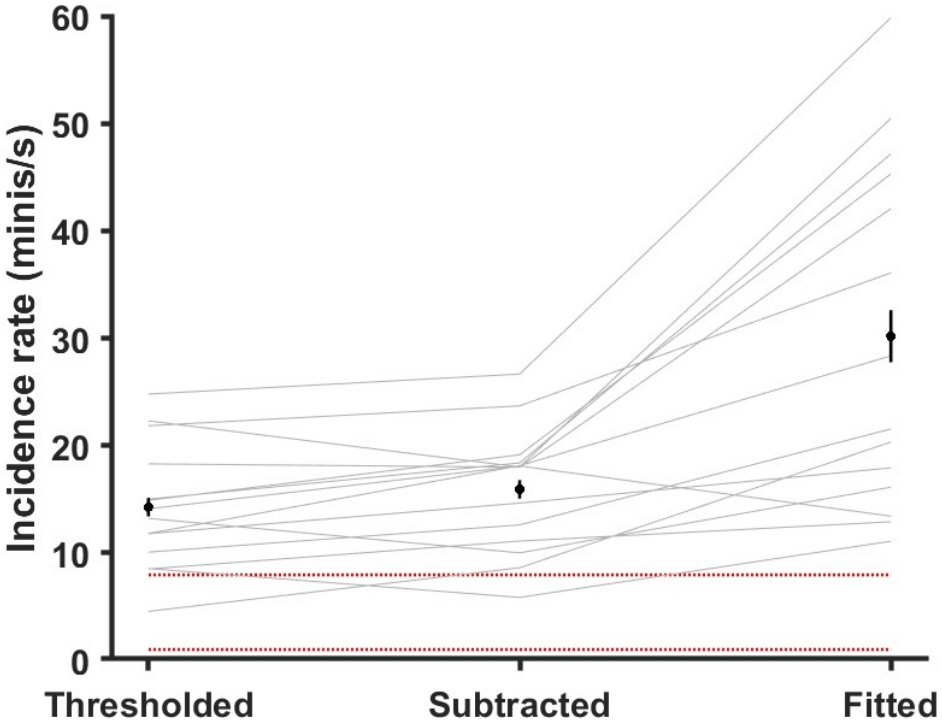

Figure 7: Estimated minis incidence rates using various methods.

'Thresholded' method: 0.8 mV detection threshold was applied to all 14 'noise + real minis' recordings and only events with larger amplitudes were included in the estimate.

'Subtracted' method: Distribution of minis-like events in the 'noise-alone' recording was subtraceted from the distribution of minis-like events in the 'noise + real minis' recording and the incidence rate estimate was based on the remaining distribution.

'Fitted' method: Simulated minis distribution was used to estimate the minis' incidence rate.

Black markers and black vertical lines correspond to means and 95% confidence intervals. Red dotted lines mark the range of incidence rates typically reported in the literature and discussed in the companion article (Dervinis and Major, 2023).

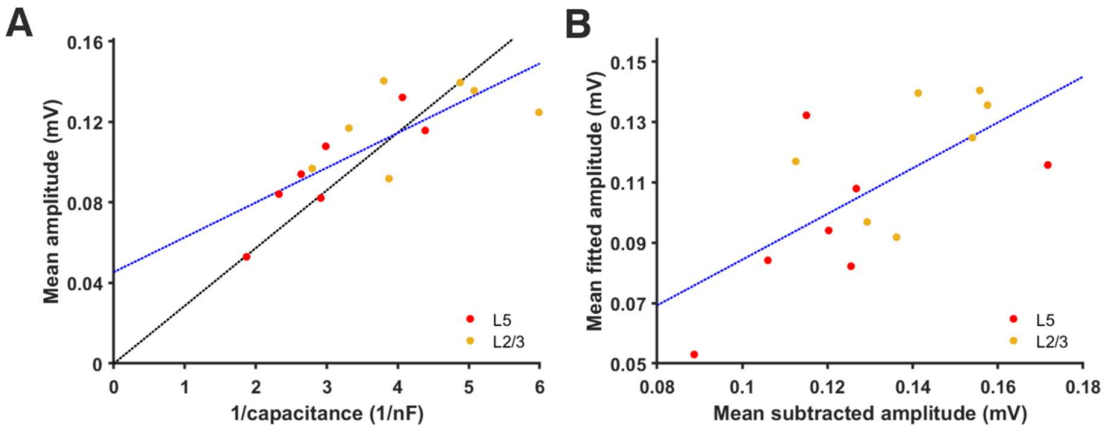

Figure 8: Relationship between cell's inverse total capacitance and estimated mean minis amplitude using simulations of minis and minis' distribution fitting.

(A) Correlation between mean minis amplitudes as derived using simulated minis' disitrbution fitting method and the inverse of cell's total capacitance. The blue line is the least square fit to the data while the black line is the fit to the data that passes through the origin of the axes.

(B) Correlation between the 'subtracted' mean minis amplitude as shown in Figure 3 and the 'fitted' mean minis amplitude.

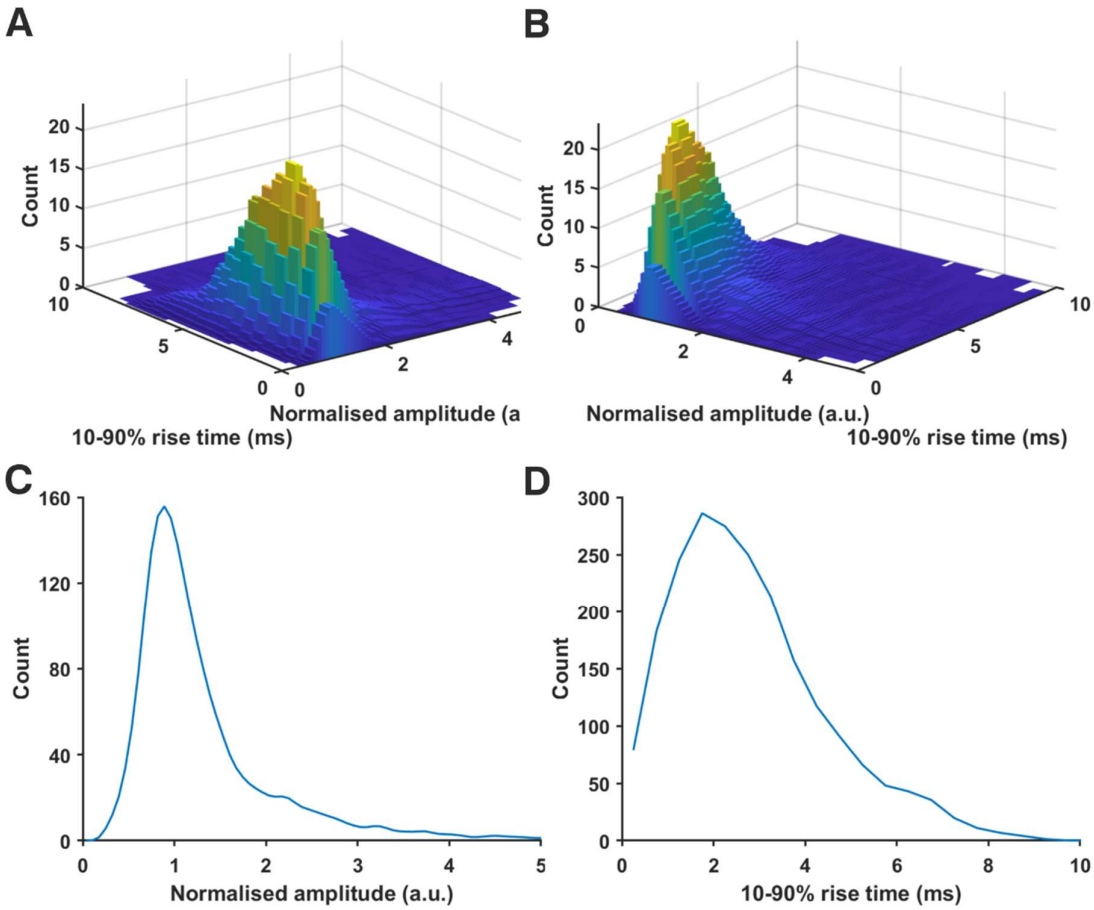

Figure 9: Generic minis distribution.

Distributions resulting from all 14 recordings were averaged and the resulting distribution was smoothed. All minis' amplitudes were normalised by means of their respective source distributions.

(A) A joint amplitude and 10-90% rise time distribution of simulated minis.

(B) The same distribution but viewed from a different angle.

(C) Marginal amplitude distribution of the same distribution as in (A).

(D) Marginal 10-90% rise time distribution of the same distribution as in (A).

Supplementary Figures

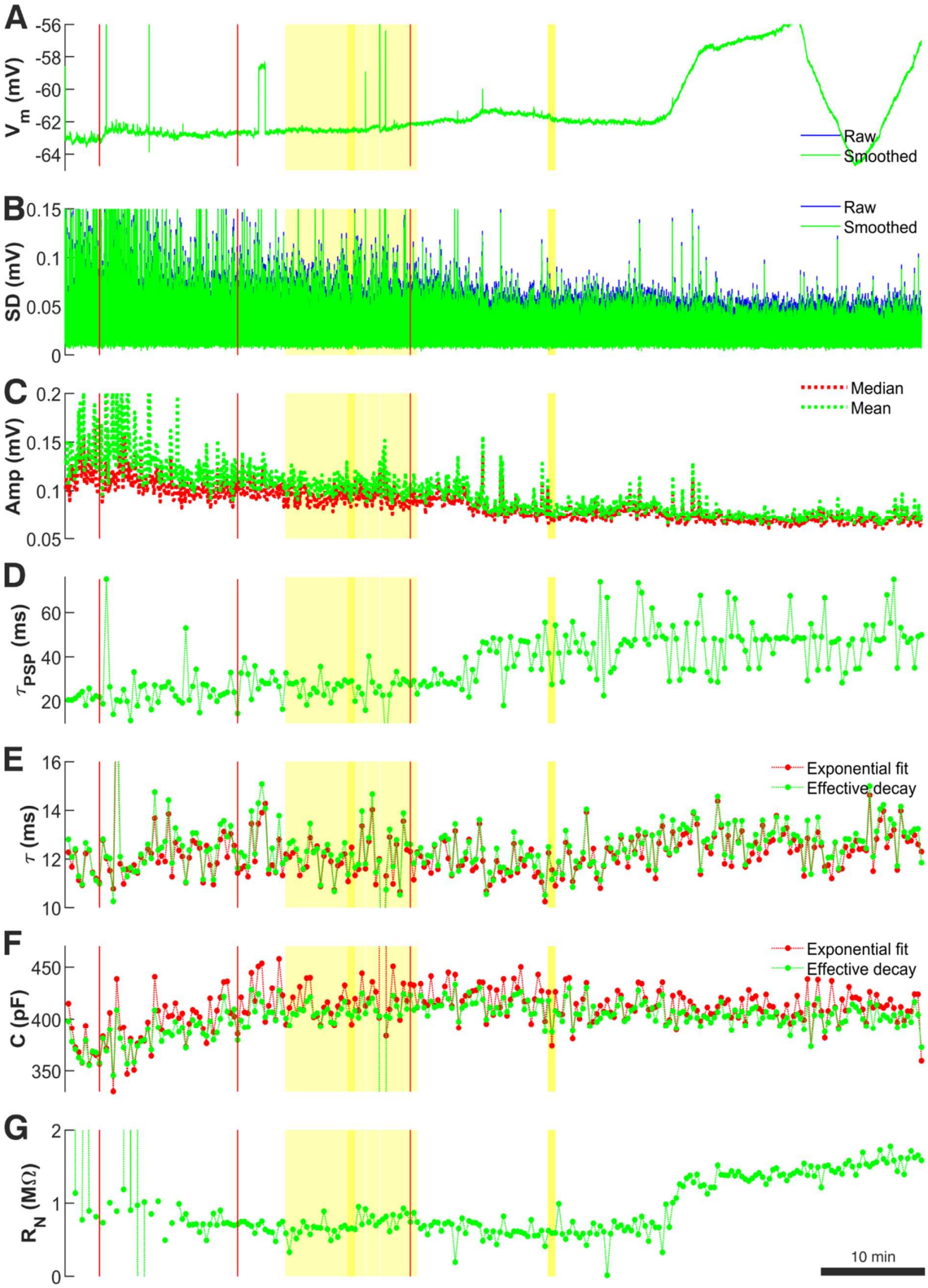

Supplementary Figure 1: Recording quality measures used during the data preprocessing stage to

select ’noise + minis’ and ’noise-alone’ recording sweeps for further data analysis for recording p106b (layer 5).

(A) Baseline V_m across the entire recording session. The raw trace is very similar to the smoothed one and, therefore, is occluded by the latter. Stimulation pulses were excluded from the display. The total recording duration (excluding pulse periods) was 4960 s. The first red vertical line marks the time when pharmacological blockade of APs was initiated. The second red vertical line marks the time when no more APs were observing in the recording. The third red vertical line marks the time when pharmacological blockade of mEPSPs was initiated. Bright yellow periods mark ‘noise + minis’ recording segment selected as the main comparison file for the distribution fitting. Light yellow marks all the remaining good quality ‘noise + minis’ recording sweeps that were also included in the distribution fitting procedure for estimating target SAD, MAD, and ‘deviation’ scores.

(B) V_m standard deviation measured over consecutive 15 ms windows over the same recording session. The meaning of symbols is the same as in panel (A).

(C) Evolution of mean and median amplitudes of the top 10% (amplitude-wise) of all detected minis-like events averaged over single sweeps across the entire recording session.

(D) Effective decay (drop to 1/e of the peak value) time constants of the same top 10% (amplitude-wise) of detected events as in panel (C) averaged over consecutive 20-second-long segments across the same session.

(E) Evolution of passive membrane time constant over the entire recording session. Measurements were averaged over consecutive 20-second-long segments. Both measurements based on exponential decay curve fit and on effective V_m drop to 1/e of the initial value were calculated and displayed.

(F) Evolution of total cell’s membrane capacitance across the recording session. Measurements were averaged over consecutive 20-second-long segments. Both measurements based on exponential decay curve fit and on effective V_m drop to 1/e of the initial value were calculated and displayed.

795 (G) Evolution of cell's input resistance (the bridge balance error) across the recording session.

796 Measurements were averaged over consecutive 20-second-long segments.

797

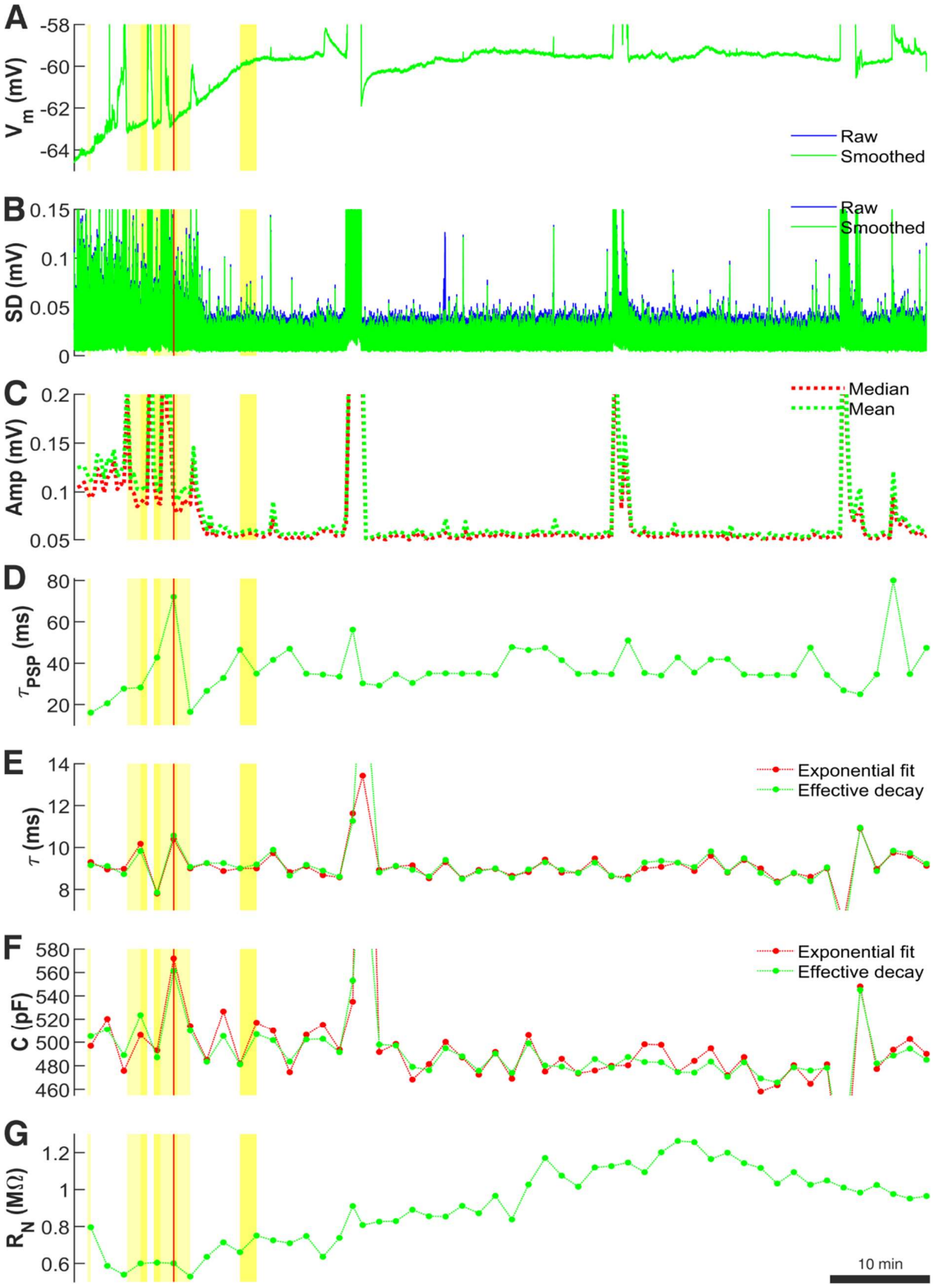

Supplementary Figure 2: Recording quality measures used during the data preprocessing stage to

800 select ’noise + minis’ and ’noise-alone’ recording sweeps for further data analysis for recording
801 p108a (layer 5).
802 The meaning of panels A-G is explained in Supplementary figure 1 except for data being averaged
803 over 100-second-long windows in panels D-G. The figure shows only part of the recording following
804 the blockade of APs with only a single red vertical time marker visible indicating the time when
805 pharmacological EPSP blockers were infused. The total duration of the recording shown in the figure
806 was 5140 s.
807

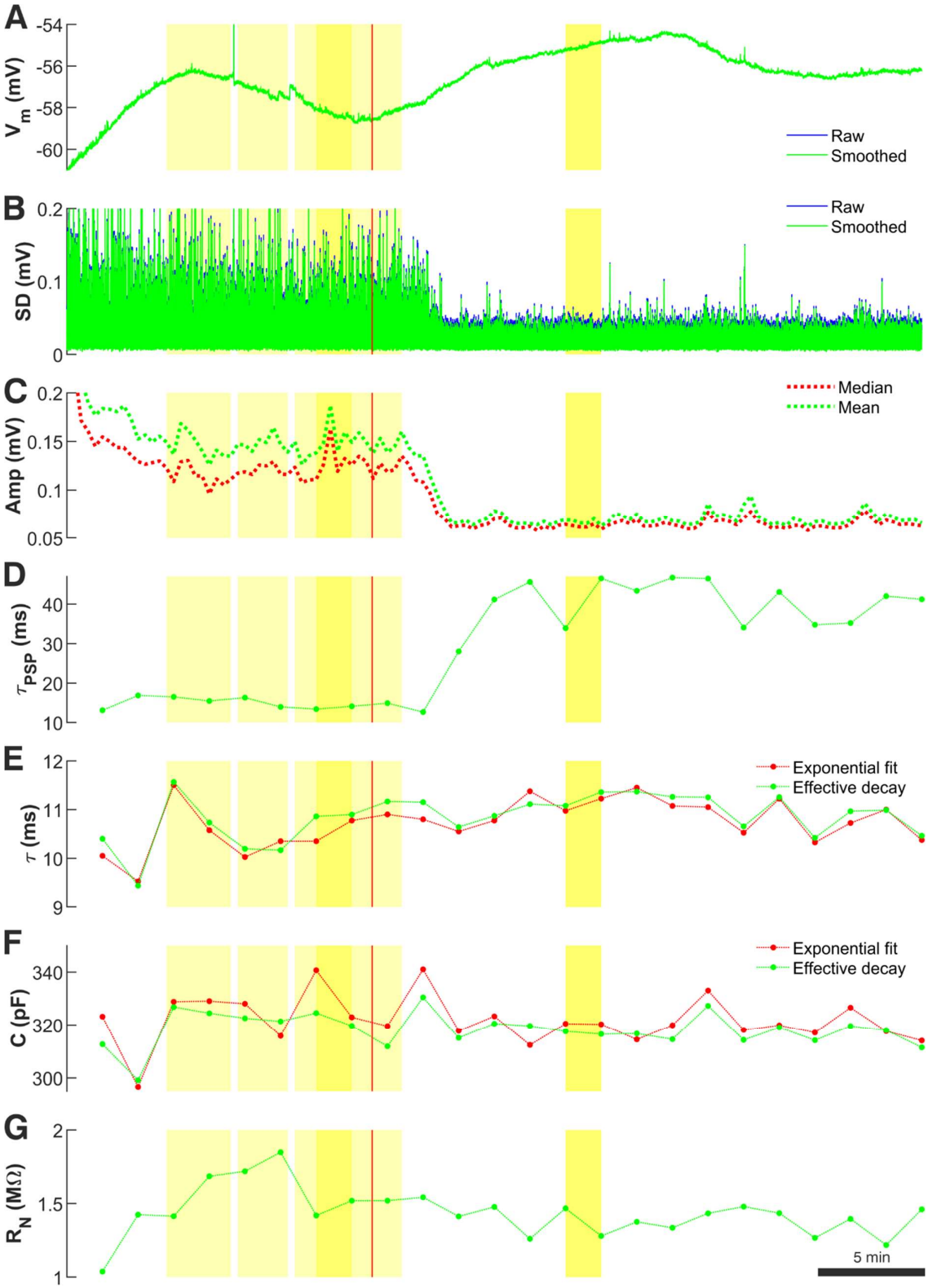

Supplementary Figure 3: Recording quality measures used during the data preprocessing stage to

select ’noise + minis’ and ’noise-alone’ recording sweeps for further data analysis for recording p108b (layer 5).

The meaning of panels A-G is explained in Supplementary figure 1 except for data being averaged over 100-second-long windows in panels D-G. The figure shows only part of the recording following the blockade of APs with only a single red vertical time marker visible indicating the time when pharmacological EPSP blockers were infused. The total duration of the recording shown in the figure was 2400 s.

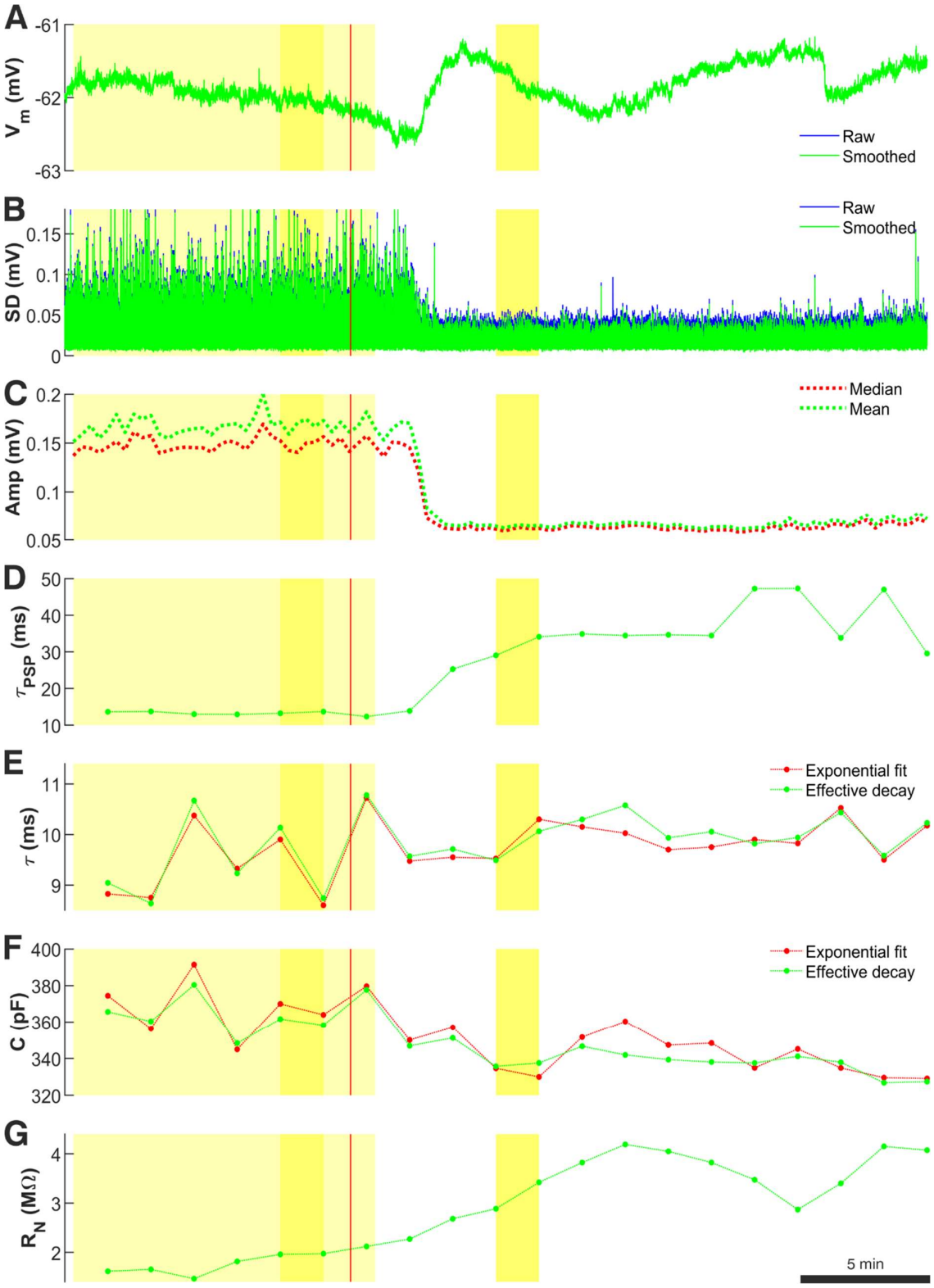

Supplementary Figure 4: Recording quality measures used during the data preprocessing stage to

820 select ’noise + minis’ and ’noise-alone’ recording sweeps for further data analysis for recording
821 p108c (layer 5).
822 The meaning of panels A-G is explained in Supplementary figure 1 except for data being averaged
823 over 100-second-long windows in panels D-G. The figure shows only part of the recording following
824 the blockade of APs with only a single red vertical time marker visible indicating the time when
825 pharmacological EPSP blockers were infused. The total duration of the recording shown in the figure
826 was 2000 s.
827

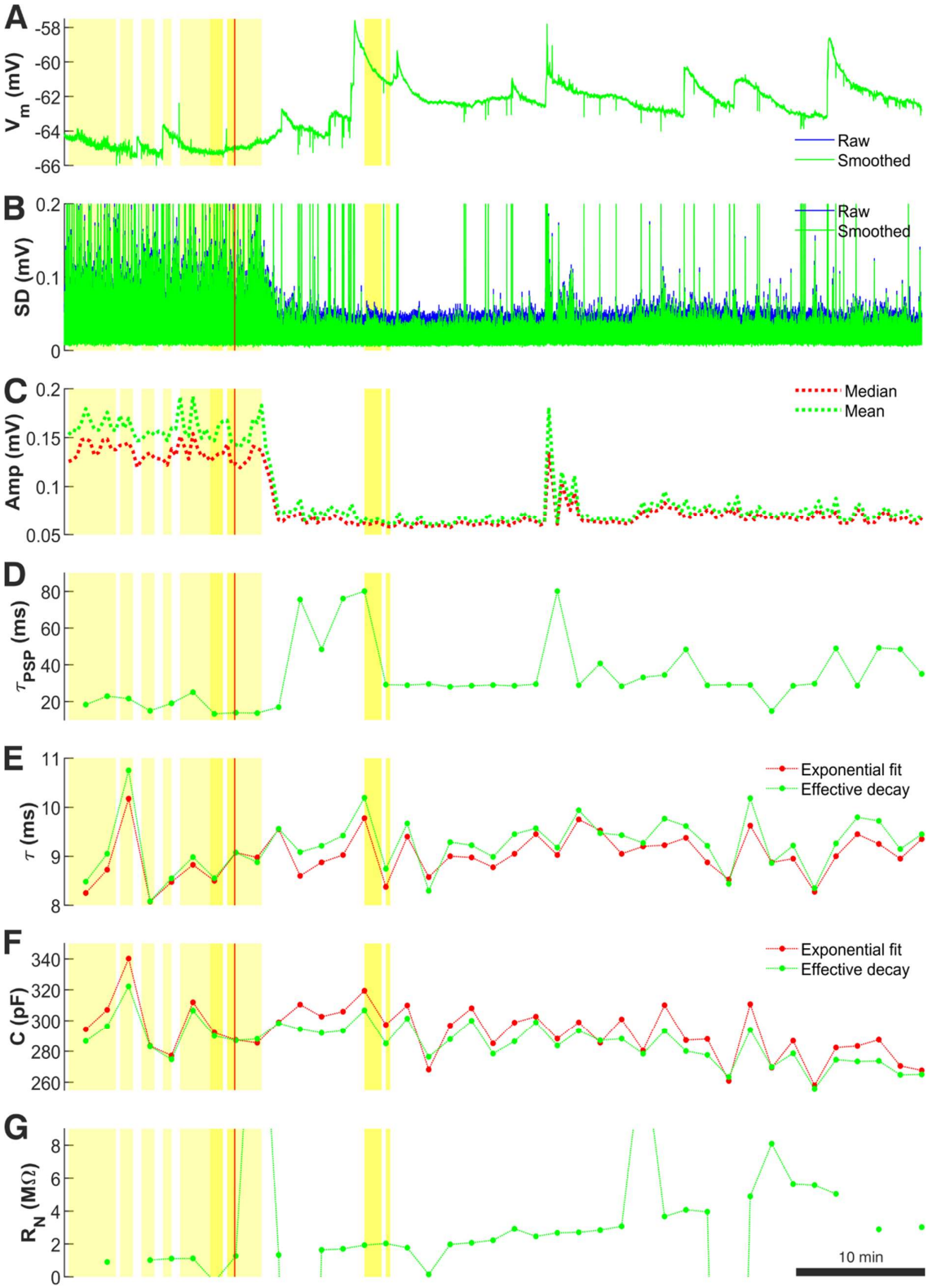

Supplementary Figure 5: Recording quality measures used during the data preprocessing stage to

select ’noise + minis’ and ’noise-alone’ recording sweeps for further data analysis for recording p120b (layer 2/3).

The meaning of panels A-G is explained in Supplementary figure 1 except for data being averaged over 100-second-long windows in panels D-G. The figure shows only part of the recording following the blockade of APs with only a single red vertical time marker visible indicating the time when pharmacological EPSP blockers were infused. The total duration of the recording shown in the figure was 4000 s.

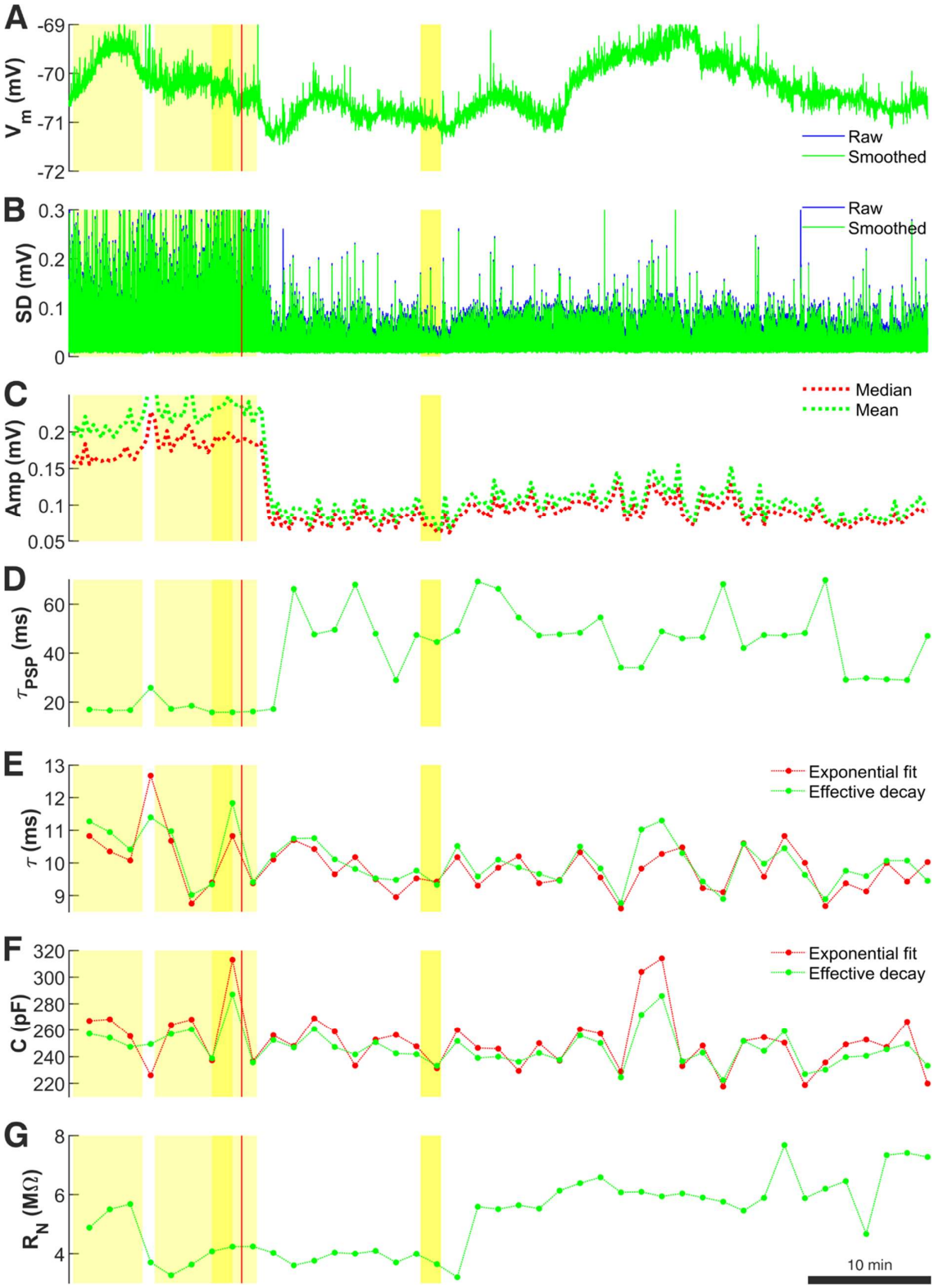

Supplementary Figure 6: Recording quality measures used during the data preprocessing stage to

840 select ’noise + minis’ and ’noise-alone’ recording sweeps for further data analysis for recording
841 p122a (layer 2/3).
842 The meaning of panels A-G is explained in Supplementary figure 1 except for data being averaged
843 over 100-second-long windows in panels D-G. The figure shows only part of the recording following
844 the blockade of APs with only a single red vertical time marker visible indicating the time when
845 pharmacological EPSP blockers were infused. The total duration of the recording shown in the figure
846 was 4200 s.
847

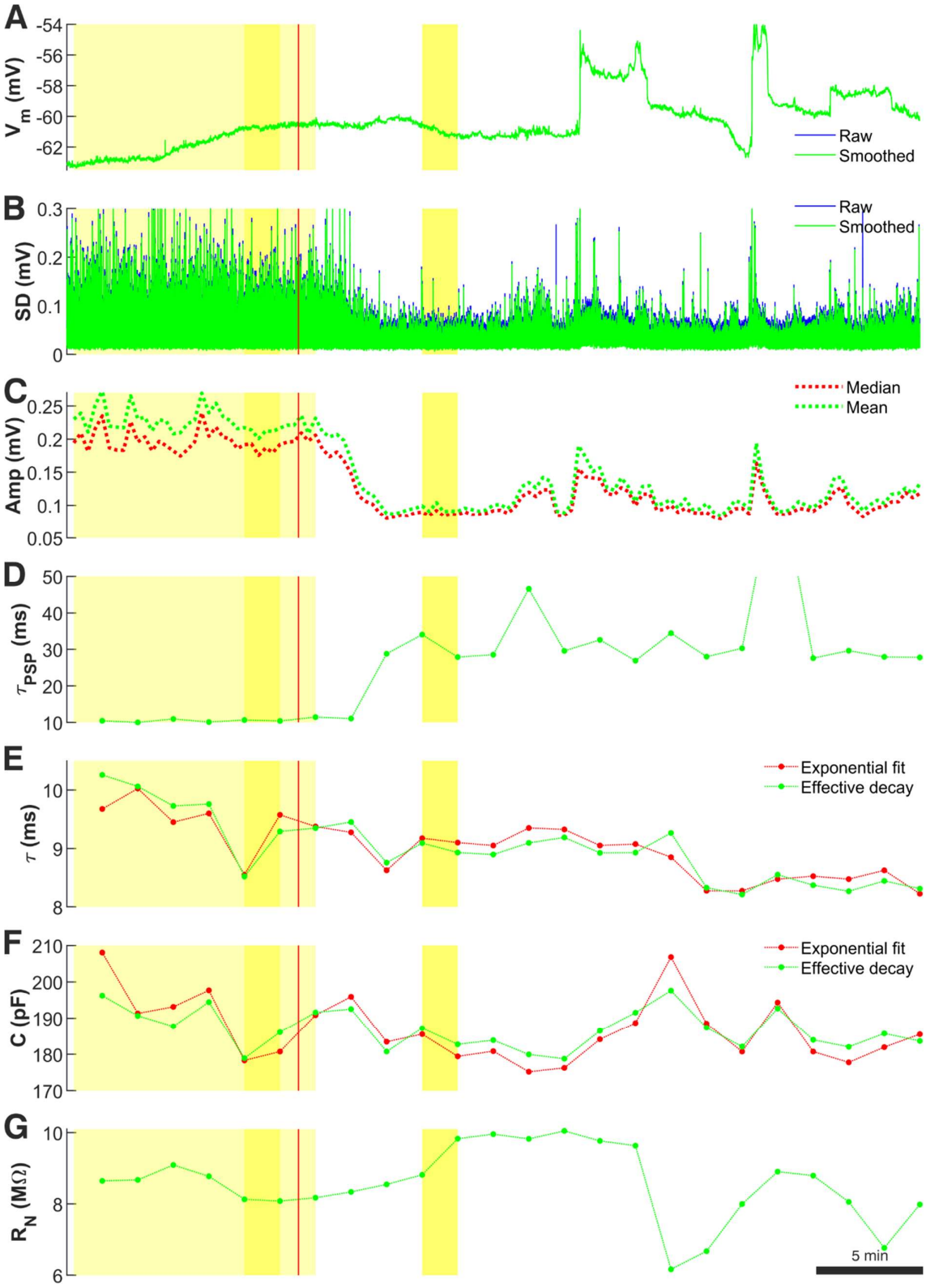

Supplementary Figure 7: Recording quality measures used during the data preprocessing stage to

select ’noise + minis’ and ’noise-alone’ recording sweeps for further data analysis for recording p124b (layer 5).

The meaning of panels A-G is explained in Supplementary figure 1 except for data being averaged over 100-second-long windows in panels D-G. The figure shows only part of the recording following the blockade of APs with only a single red vertical time marker visible indicating the time when pharmacological EPSP blockers were infused. The total duration of the recording shown in the figure was 2400 s.

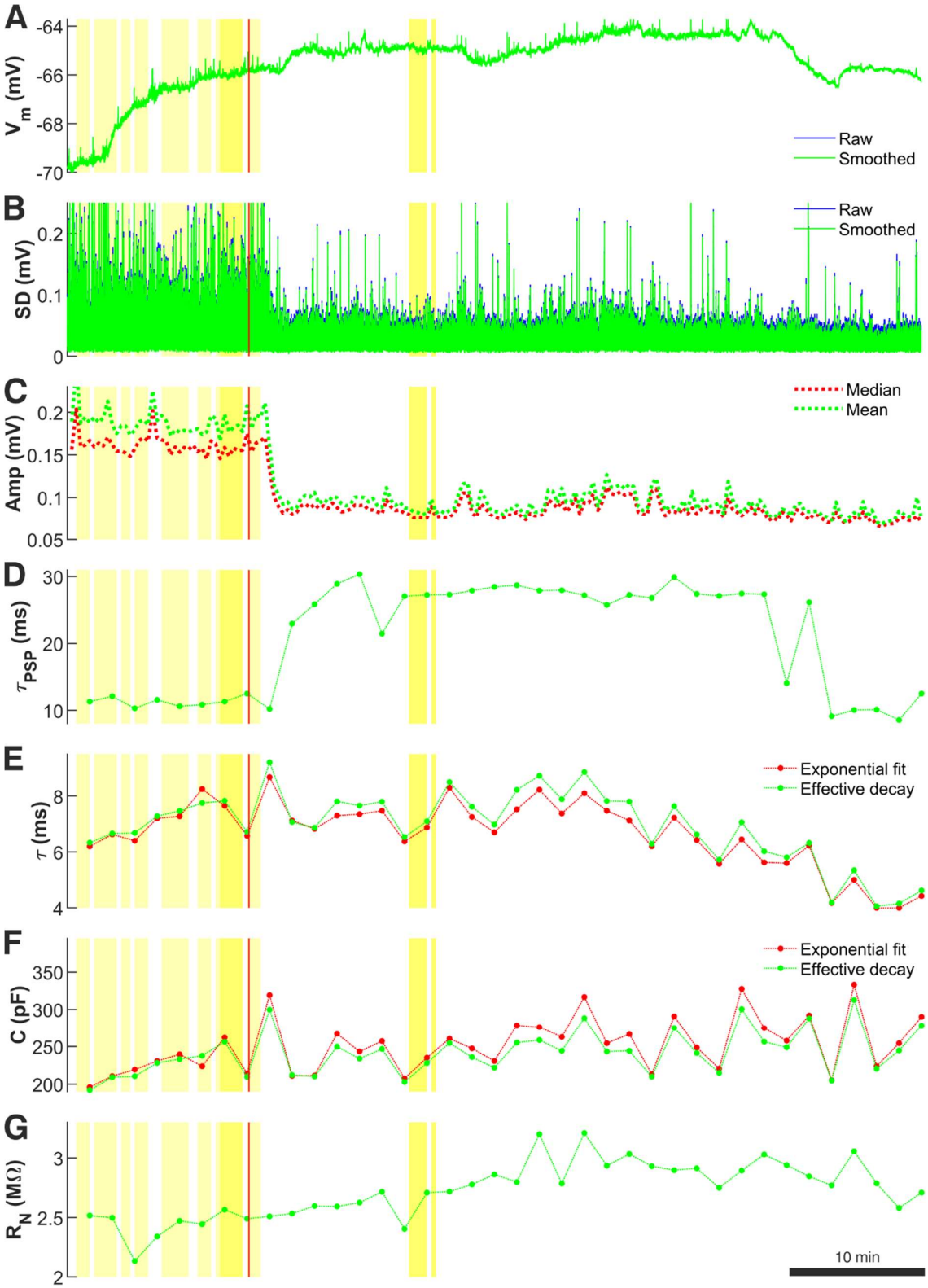

Supplementary Figure 8: Recording quality measures used during the data preprocessing stage to

select ’noise + minis’ and ’noise-alone’ recording sweeps for further data analysis for recording p125a (layer 2/3).

The meaning of panels A-G is explained in Supplementary figure 1 except for data being averaged over 100-second-long windows in panels D-G. The figure shows only part of the recording following the blockade of APs with only a single red vertical time marker visible indicating the time when pharmacological EPSP blockers were infused. The total duration of the recording shown in the figure was 3800 s.

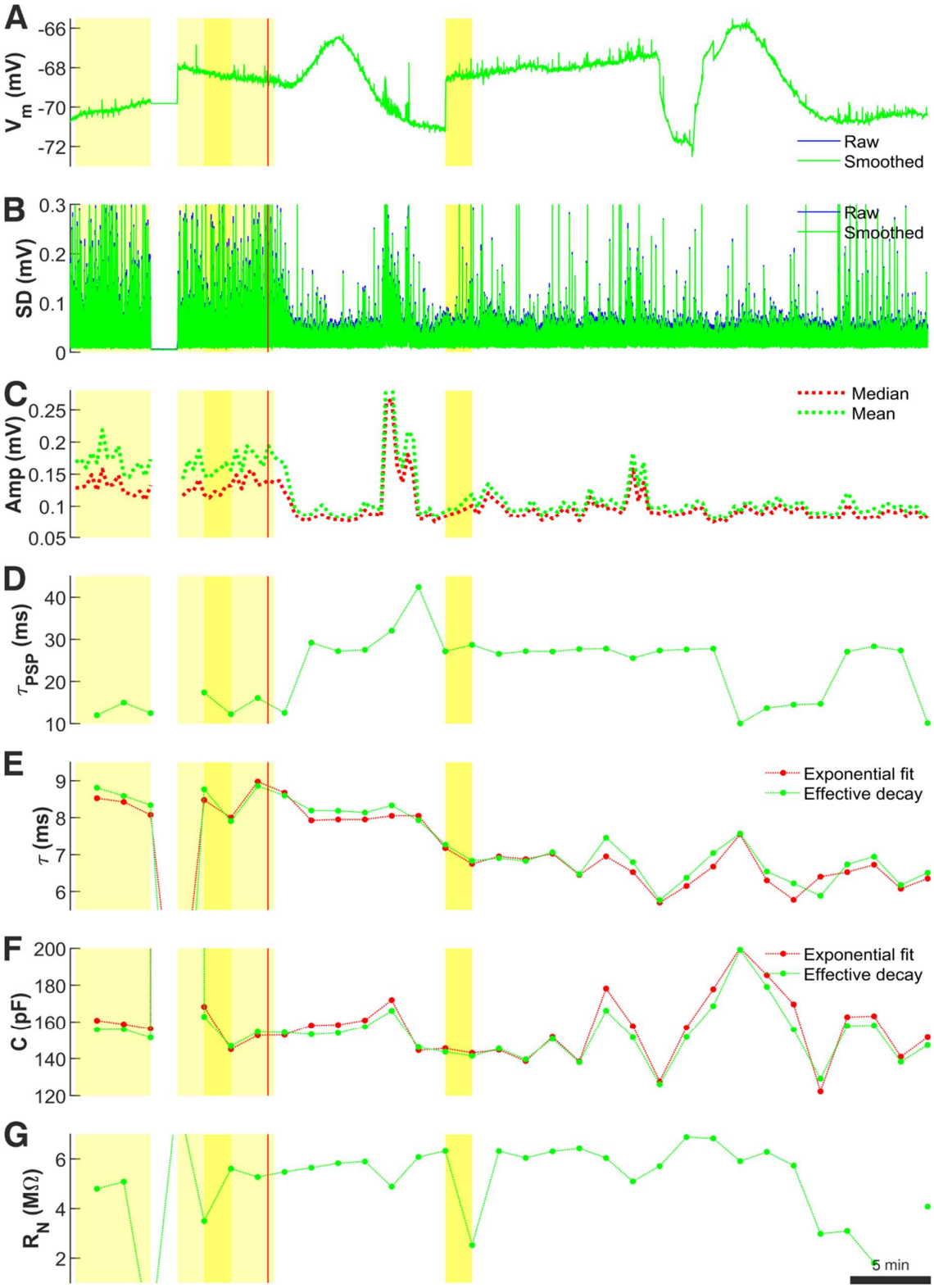

Supplementary Figure 9: Recording quality measures used during the data preprocessing stage to

select ’noise + minis’ and ’noise-alone’ recording sweeps for further data analysis for recording p127c (layer 2/3).

The meaning of panels A-G is explained in Supplementary figure 1 except for data being averaged over 100-second-long windows in panels D-G. The figure shows only part of the recording following the blockade of APs with only a single red vertical time marker visible indicating the time when pharmacological EPSP blockers were infused. The total duration of the recording shown in the figure was 3200 s.

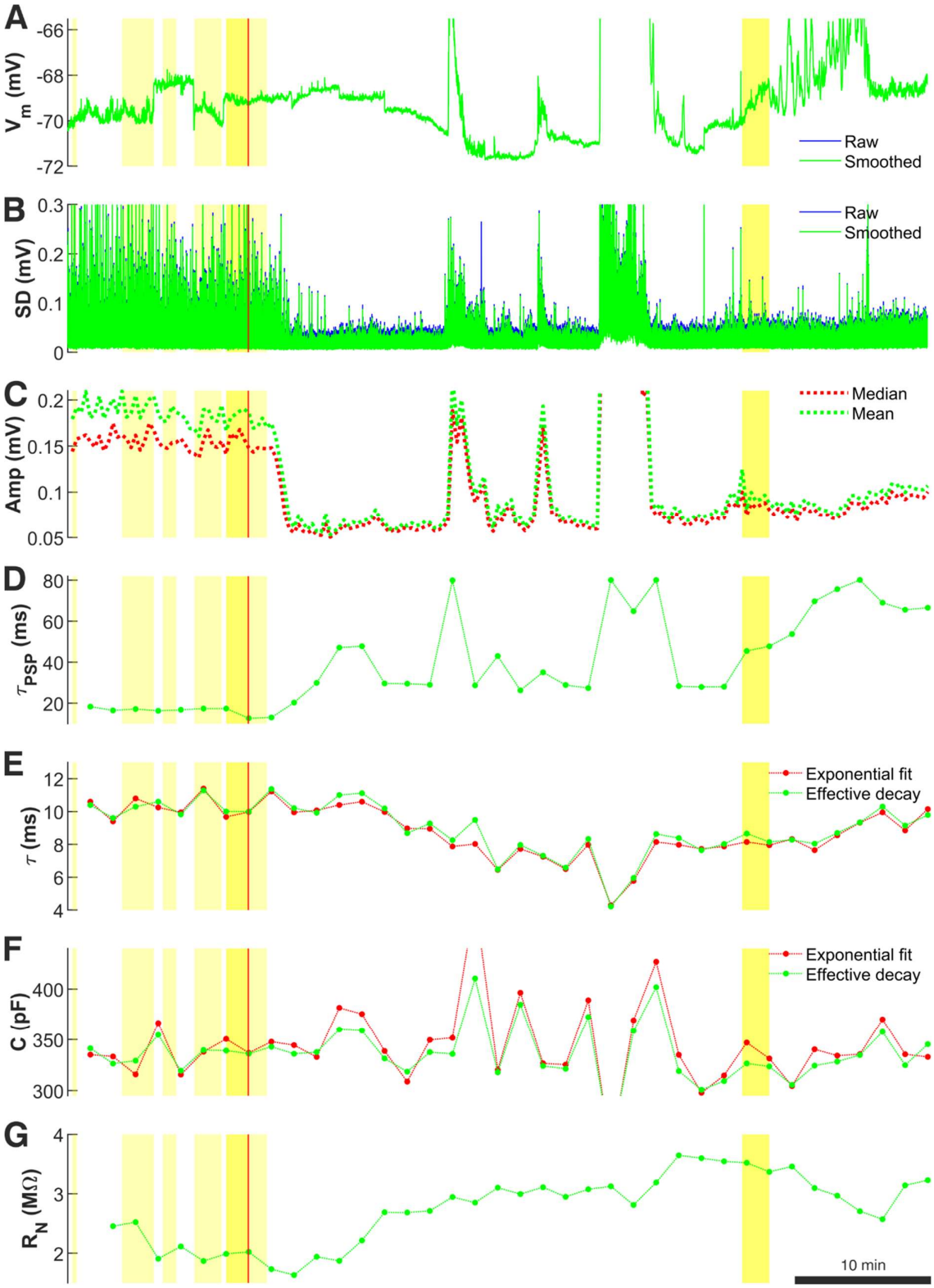

Supplementary Figure 11: Recording quality measures used during the data preprocessing stage to

880 select ’noise + minis’ and ’noise-alone’ recording sweeps for further data analysis for recording
881 p129a (layer 5).
882 The meaning of panels A-G is explained in Supplementary figure 1 except for data being averaged
883 over 100-second-long windows in panels D-G. The figure shows only part of the recording following
884 the blockade of APs with only a single red vertical time marker visible indicating the time when
885 pharmacological EPSP blockers were infused. The total duration of the recording shown in the figure
886 was 4000 s.
887

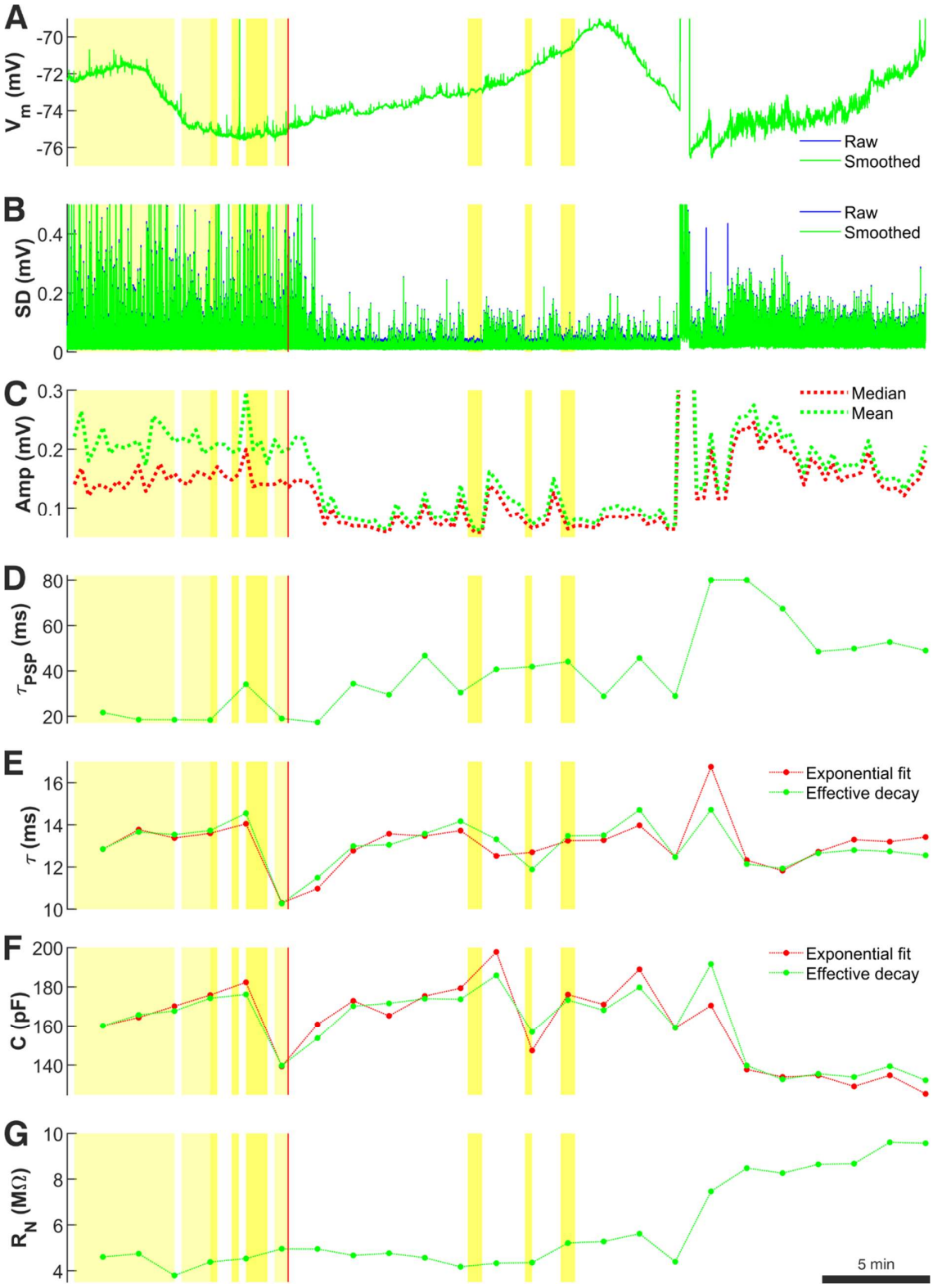

Supplementary Figure 12: Recording quality measures used during the data preprocessing stage to

890 select ’noise + minis’ and ’noise-alone’ recording sweeps for further data analysis for recording
891 p131a (layer 2/3).
892 The meaning of panels A-G is explained in Supplementary figure 1 except for data being averaged
893 over 100-second-long windows in panels D-G. The figure shows only part of the recording following
894 the blockade of APs with only a single red vertical time marker visible indicating the time when
895 pharmacological EPSP blockers were infused. The total duration of the recording shown in the figure
896 was 2400 s.
897

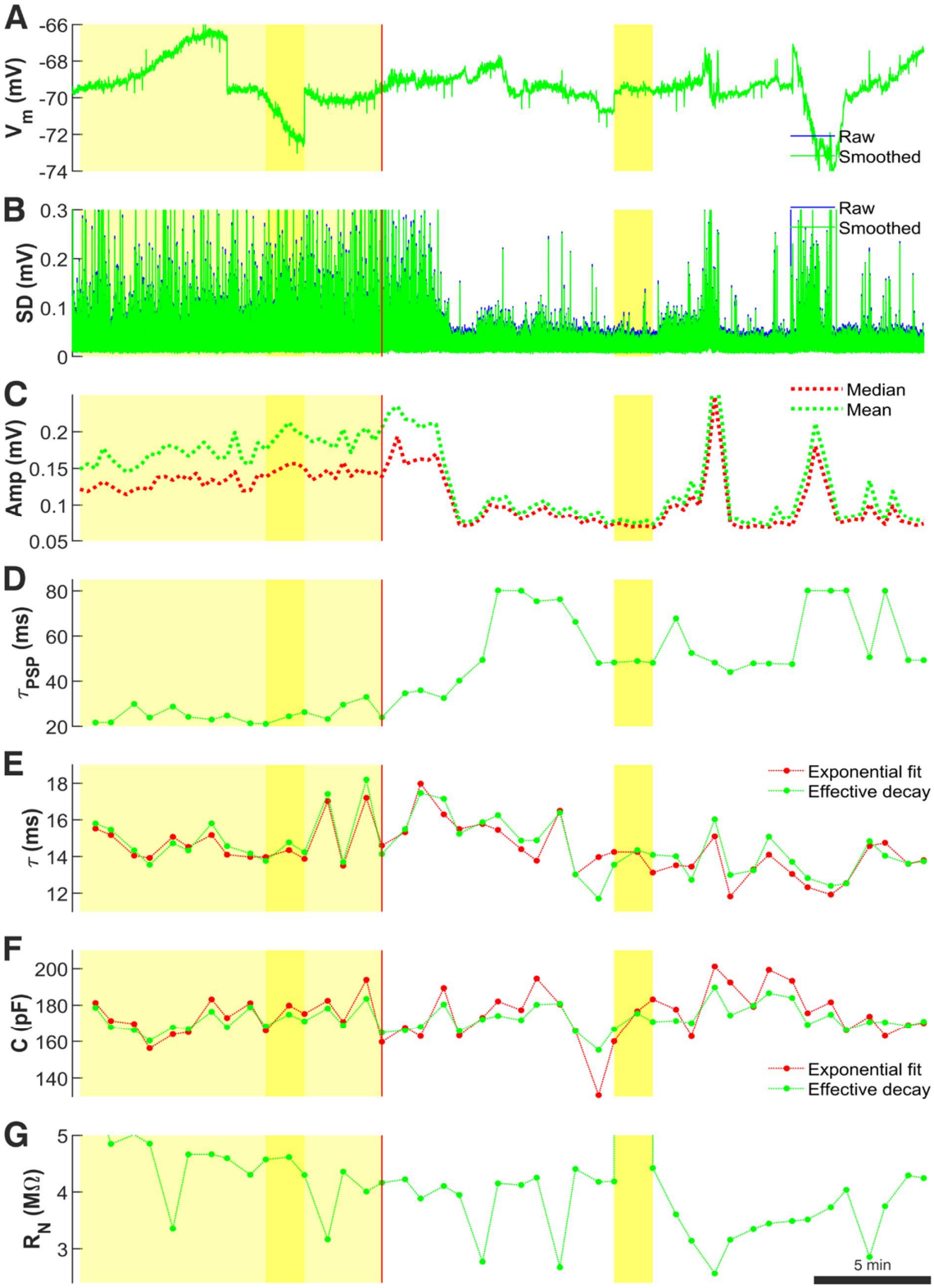

Supplementary Figure 13: Recording quality measures used during the data preprocessing stage to

900 select ’noise + minis’ and ’noise-alone’ recording sweeps for further data analysis for recording
901 p131c (layer 2/3).
902 The meaning of panels A-G is explained in Supplementary figure 1 except for data being averaged
903 over 100-second-long windows in panels D-G. The figure shows only part of the recording following
904 the blockade of APs with only a single red vertical time marker visible indicating the time when
905 pharmacological EPSP blockers were infused. The total duration of the recording shown in the figure
906 was 2200 s.
907

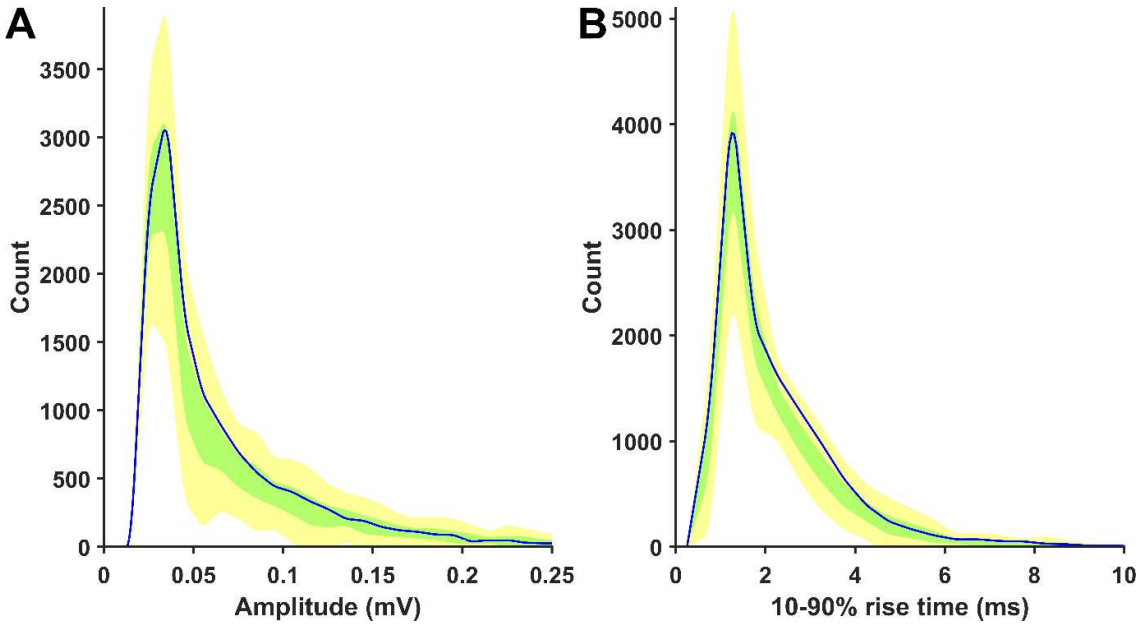

Supplementary figure 14: Distributions of minis-like events detected in a ’noise + simulated minis’ voltage trace that closely matched ‘noise + real minis‘ recordings.

Parameters of simulated minis were controlled by the GA, whereas the ’noise-alone’ recording was obtained in cell p103a of the cortical layer 5. Interval marked by green indicates the range of values across multiple ‘noise + real minis’ recording files. The yellow shaded interval indicates the triple size range.

(A) Amplitude distribution of minis-like events detected in a ’noise + simulated minis’ voltage trace (the blue curve).

(B) 10-90% rise time distribution of minis-like events detected in a ’noise + simulated minis’ voltage trace (the blue curve).

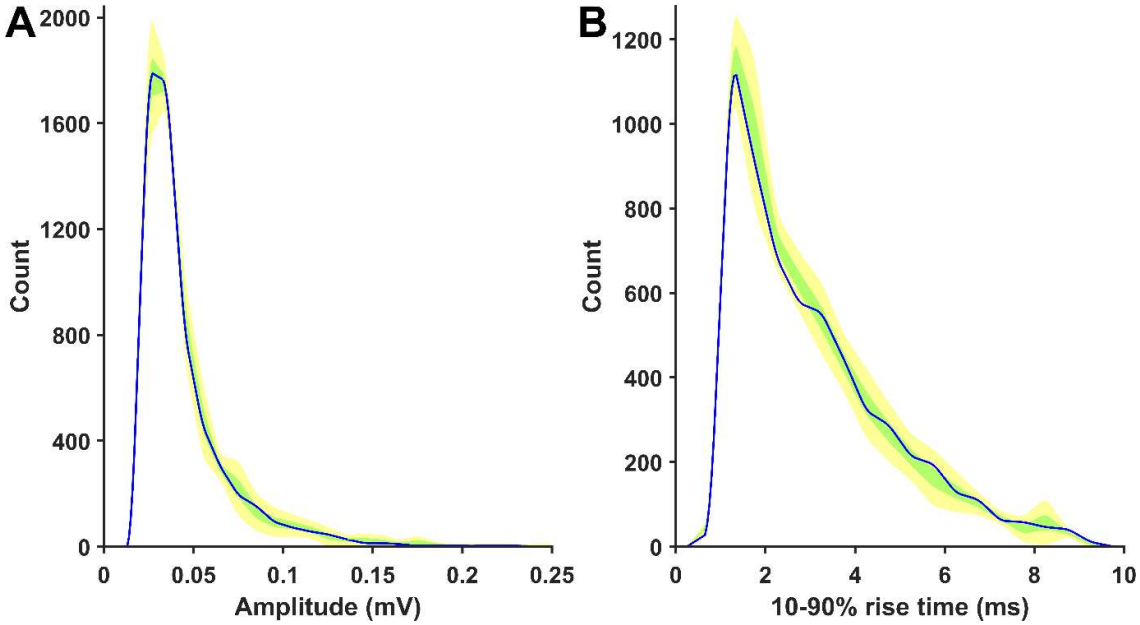

Supplementary figure 15: Distributions of minis-like events detected in a ’noise + simulated minis’ voltage trace that closely matched ‘noise + real minis‘ recordings. Parameters of simulated minis were controlled by the GA, whereas the ’noise-alone’ recording was obtained in cell p108a of the cortical layer 5. The meaning of the two panels and different colours is explained in Supplementary figure 14.

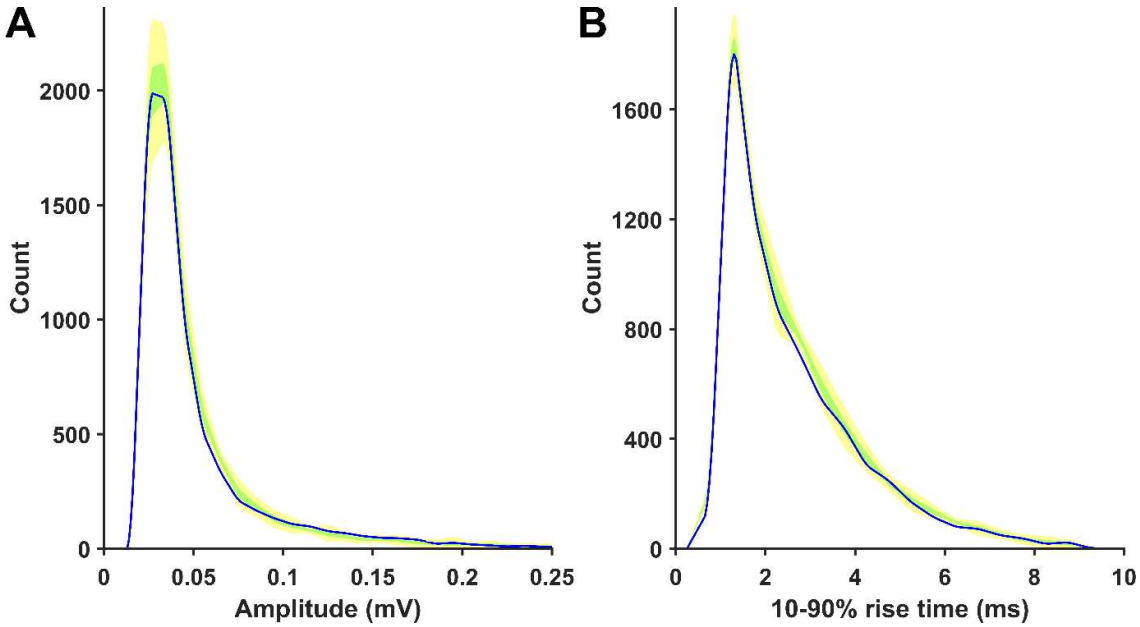

927

928 **Supplementary figure 16:** Distributions of minis-like events detected in a ’noise + simulated minis’

929 voltage trace that closely matched ‘noise + real minis‘ recordings.

930 Parameters of simulated minis were controlled by the GA, whereas the ’noise-alone’ recording was

931 obtained in cell p108b of the cortical layer 5. The meaning of the two panels and different colours is

932 explained in Supplementary figure 14.

933

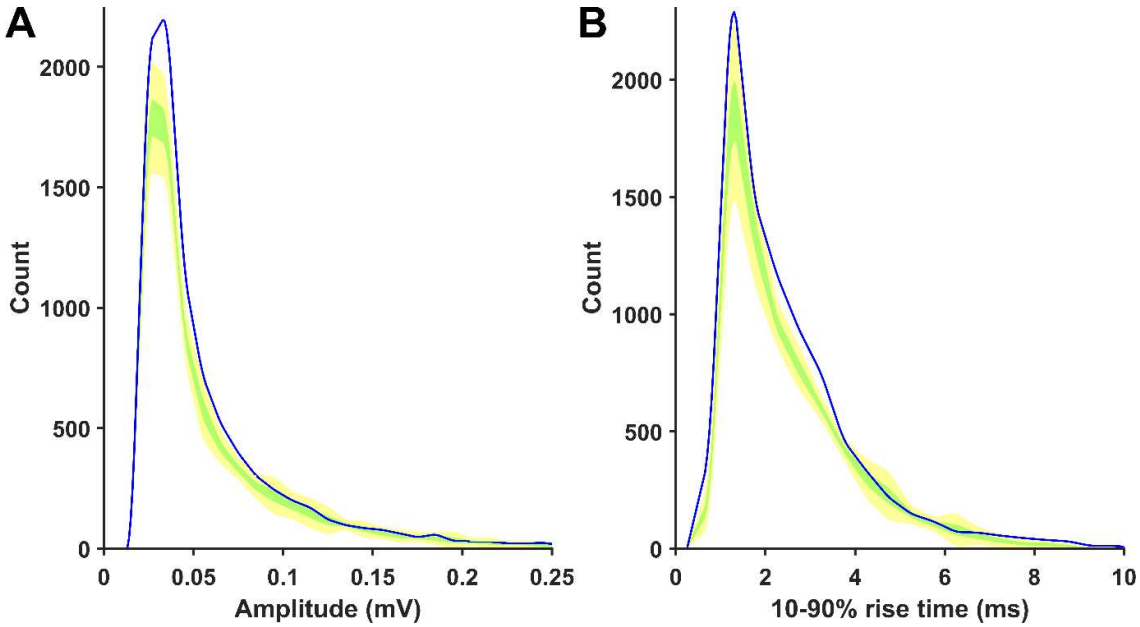

Supplementary figure 17: Distributions of minis-like events detected in a ’noise + simulated minis’ voltage trace that closely matched ‘noise + real minis‘ recordings. Parameters of simulated minis were controlled by the GA, whereas the ’noise-alone’ recording was obtained in cell p108c of the cortical layer 5. The meaning of the two panels and different colours is explained in Supplementary figure 14.

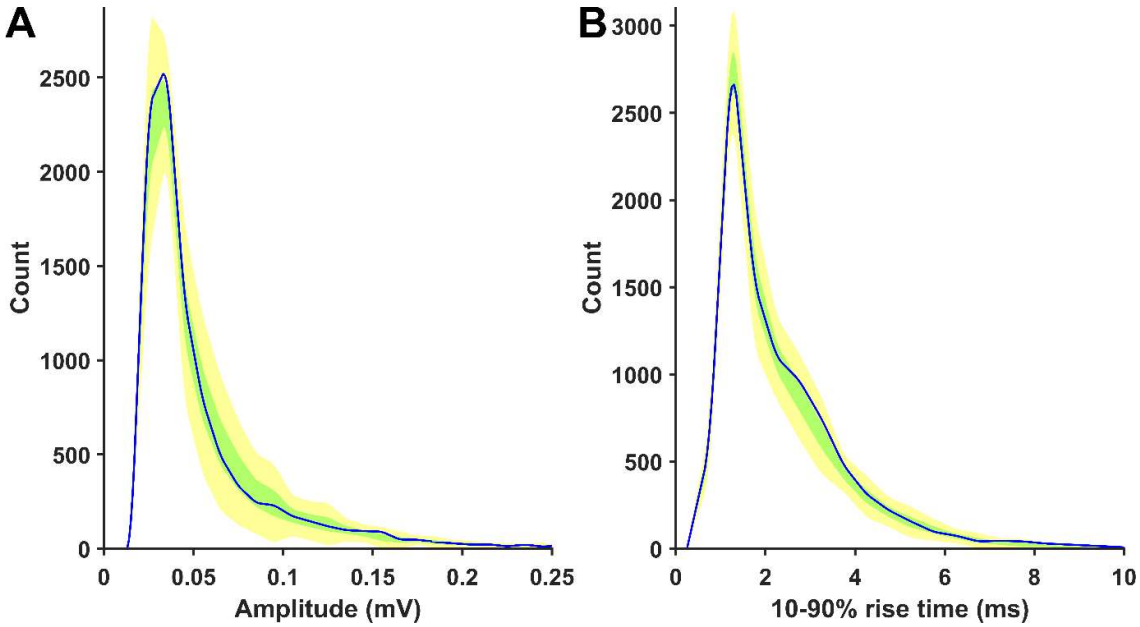

Supplementary figure 18: Distributions of minis-like events detected in a ’noise + simulated minis’ voltage trace that closely matched ‘noise + real minis‘ recordings. Parameters of simulated minis were controlled by the GA, whereas the ’noise-alone’ recording was obtained in cell p120b of the cortical layer 2/3. The meaning of the two panels and different colours is explained in Supplementary figure 14.

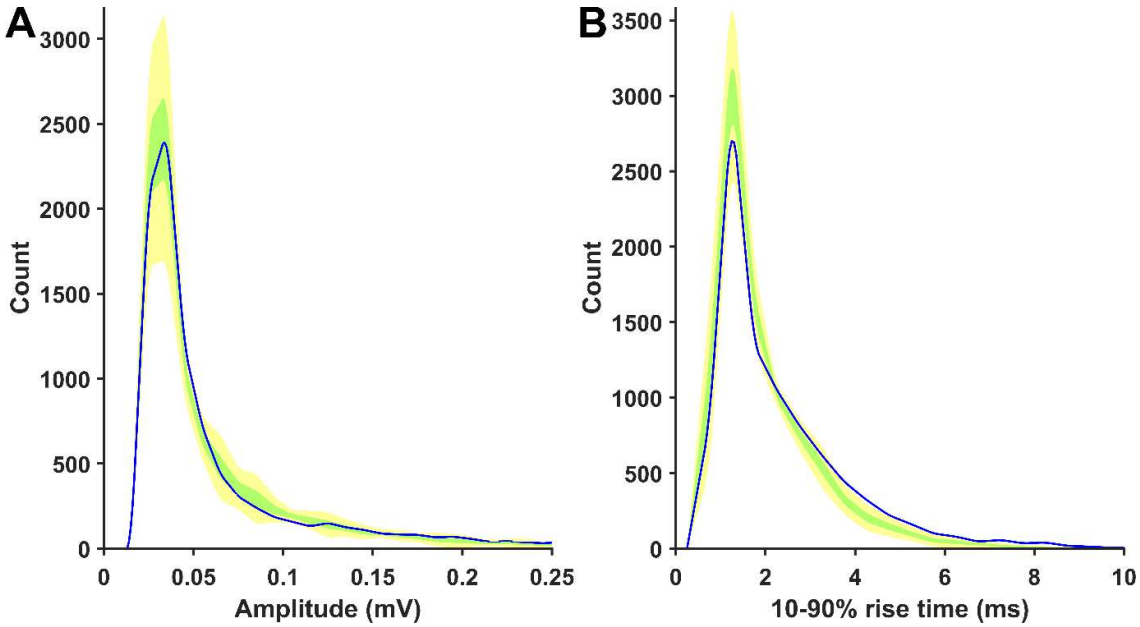

Supplementary figure 19: Distributions of minis-like events detected in a ’noise + simulated minis’ voltage trace that closely matched ‘noise + real minis‘ recordings. Parameters of simulated minis were controlled by the GA, whereas the ’noise-alone’ recording was obtained in cell p122a of the cortical layer 2/3. The meaning of the two panels and different colours is explained in Supplementary figure 14.

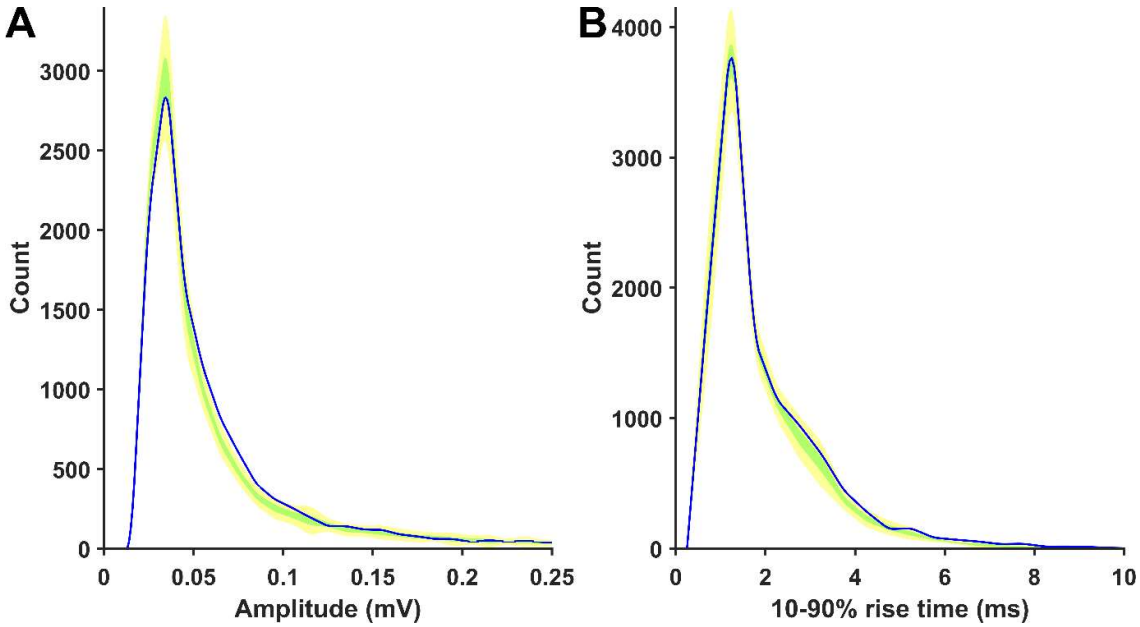

Supplementary figure 20: Distributions of minis-like events detected in a ’noise + simulated minis’ voltage trace that closely matched ‘noise + real minis‘ recordings. Parameters of simulated minis were controlled by the GA, whereas the ’noise-alone’ recording was obtained in cell p124b of the cortical layer 5. The meaning of the two panels and different colours is explained in Supplementary figure 14.

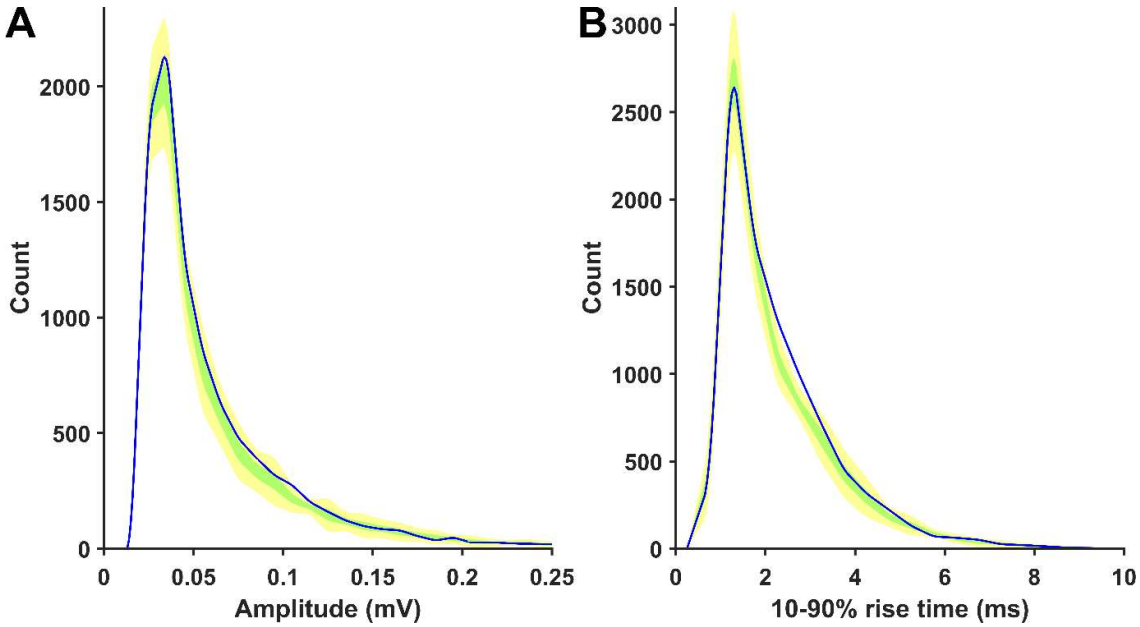

Supplementary figure 21: Distributions of minis-like events detected in a ’noise + simulated minis’ voltage trace that closely matched ‘noise + real minis‘ recordings. Parameters of simulated minis were controlled by the GA, whereas the ’noise-alone’ recording was obtained in cell p125a of the cortical layer 2/3. The meaning of the two panels and different colours is explained in Supplementary figure 14.

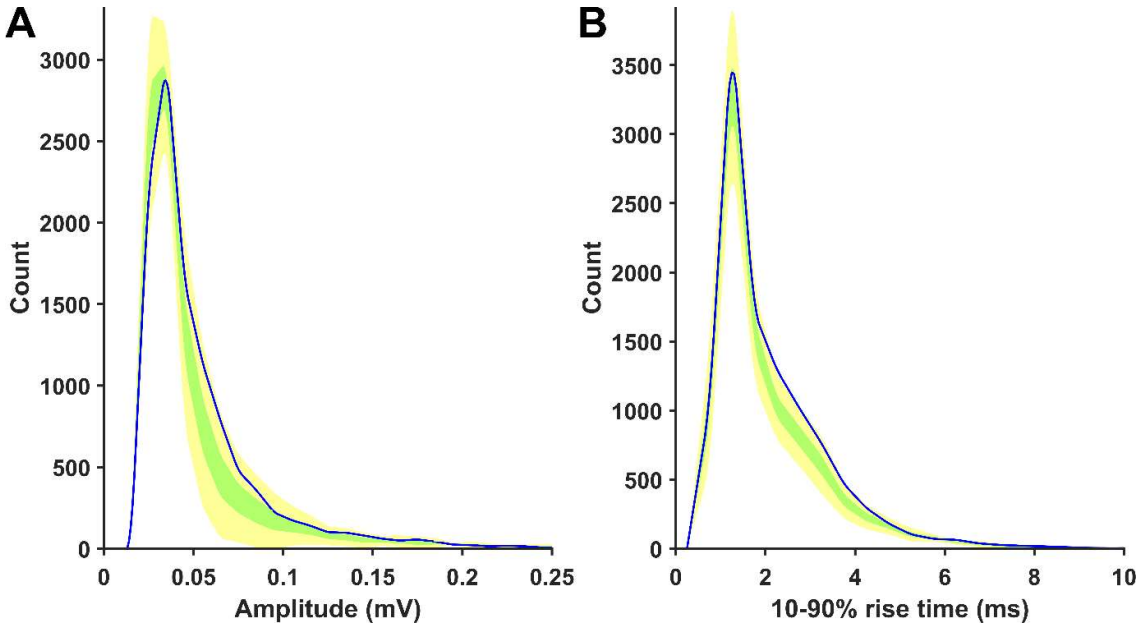

Supplementary figure 22: Distributions of minis-like events detected in a ’noise + simulated minis’ voltage trace that closely matched ‘noise + real minis‘ recordings. Parameters of simulated minis were controlled by the GA, whereas the ’noise-alone’ recording was obtained in cell p127c of the cortical layer 2/3. The meaning of the two panels and different colours is explained in Supplementary figure 14.

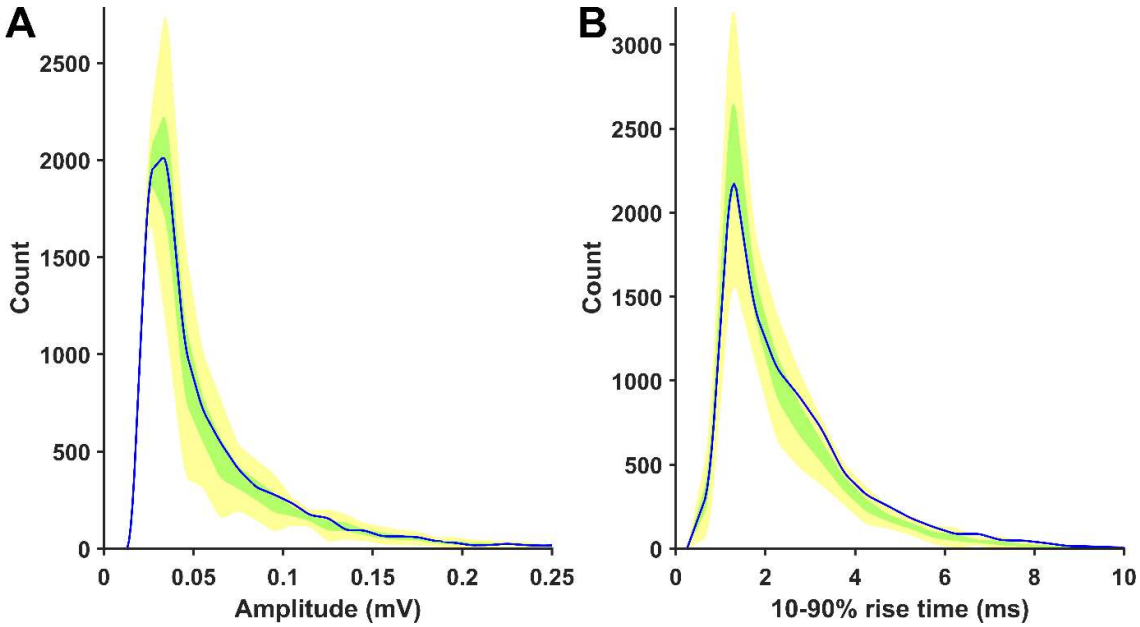

Supplementary figure 23: Distributions of minis-like events detected in a ’noise + simulated minis’ voltage trace that closely matched ‘noise + real minis‘ recordings.

Parameters of simulated minis were controlled by the GA, whereas the ’noise-alone’ recording was obtained in cell p128c of the cortical layer 2/3. The meaning of the two panels and different colours is explained in Supplementary figure 14.

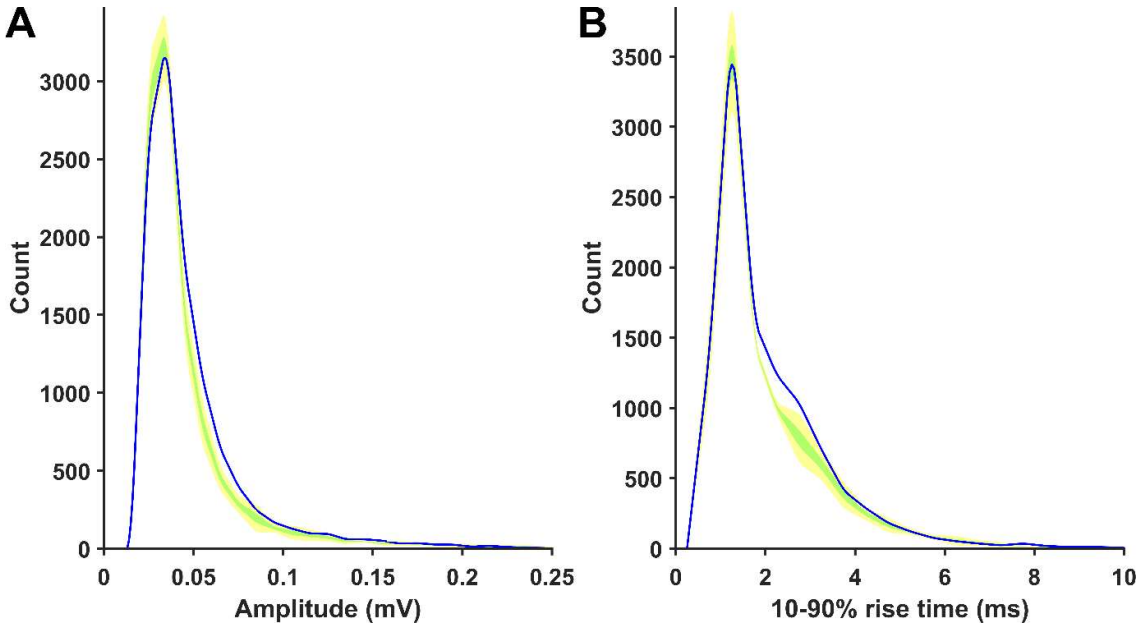

983

984 **Supplementary figure 24:** Distributions of minis-like events detected in a ’noise + simulated minis’

985 voltage trace that closely matched ‘noise + real minis‘ recordings.

986 Parameters of simulated minis were controlled by the GA, whereas the ’noise-alone’ recording was

987 obtained in cell p129a of the cortical layer 5. The meaning of the two panels and different colours is

988 explained in Supplementary figure 14.

989

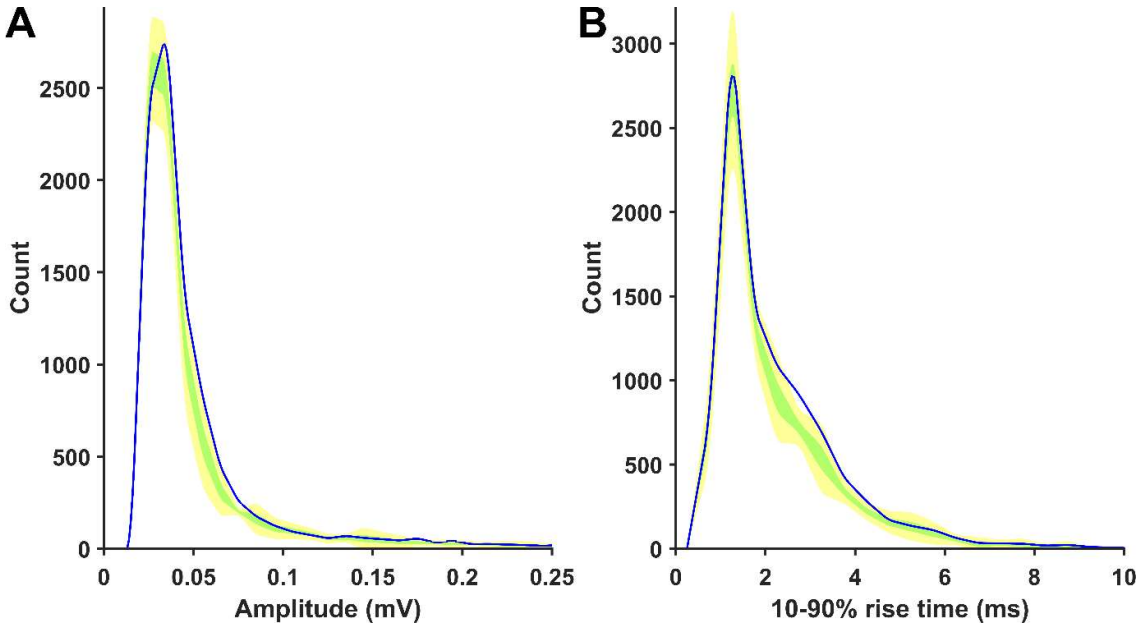

Supplementary figure 25: Distributions of minis-like events detected in a ’noise + simulated minis’ voltage trace that closely matched ‘noise + real minis‘ recordings. Parameters of simulated minis were controlled by the GA, whereas the ’noise-alone’ recording was obtained in cell p131a of the cortical layer 2/3. The meaning of the two panels and different colours is explained in Supplementary figure 14.

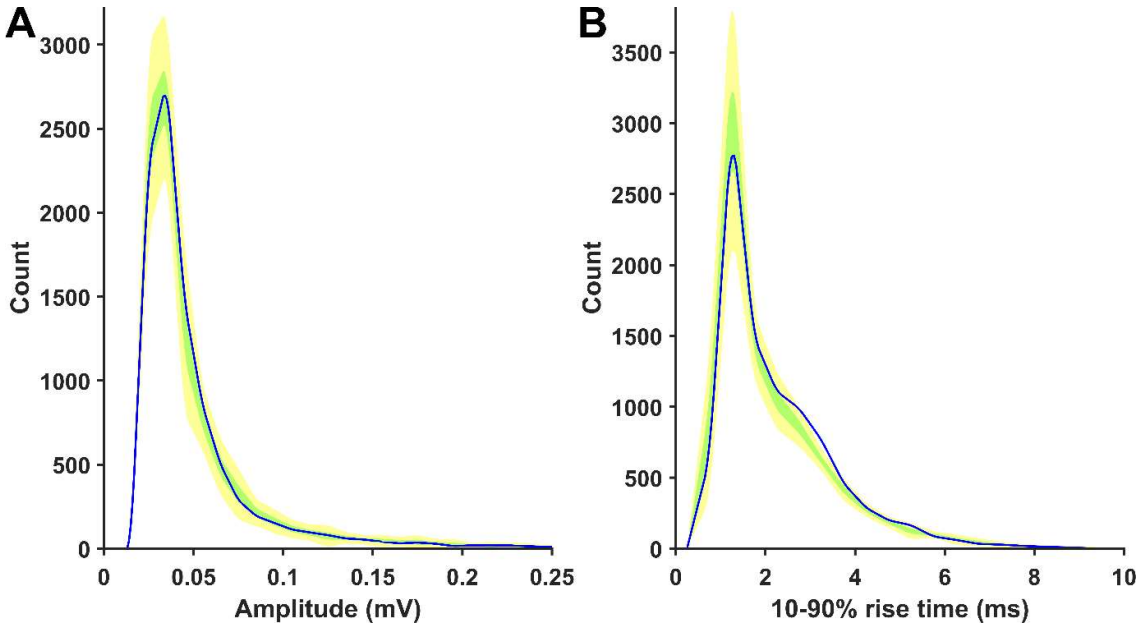

Supplementary figure 26: Distributions of minis-like events detected in a ’noise + simulated minis’ voltage trace that closely matched ‘noise + real minis‘ recordings. Parameters of simulated minis were controlled by the GA, whereas the ’noise-alone’ recording was obtained in cell p131c of the cortical layer 2/3. The meaning of the two panels and different colours is explained in Supplementary figure 14.

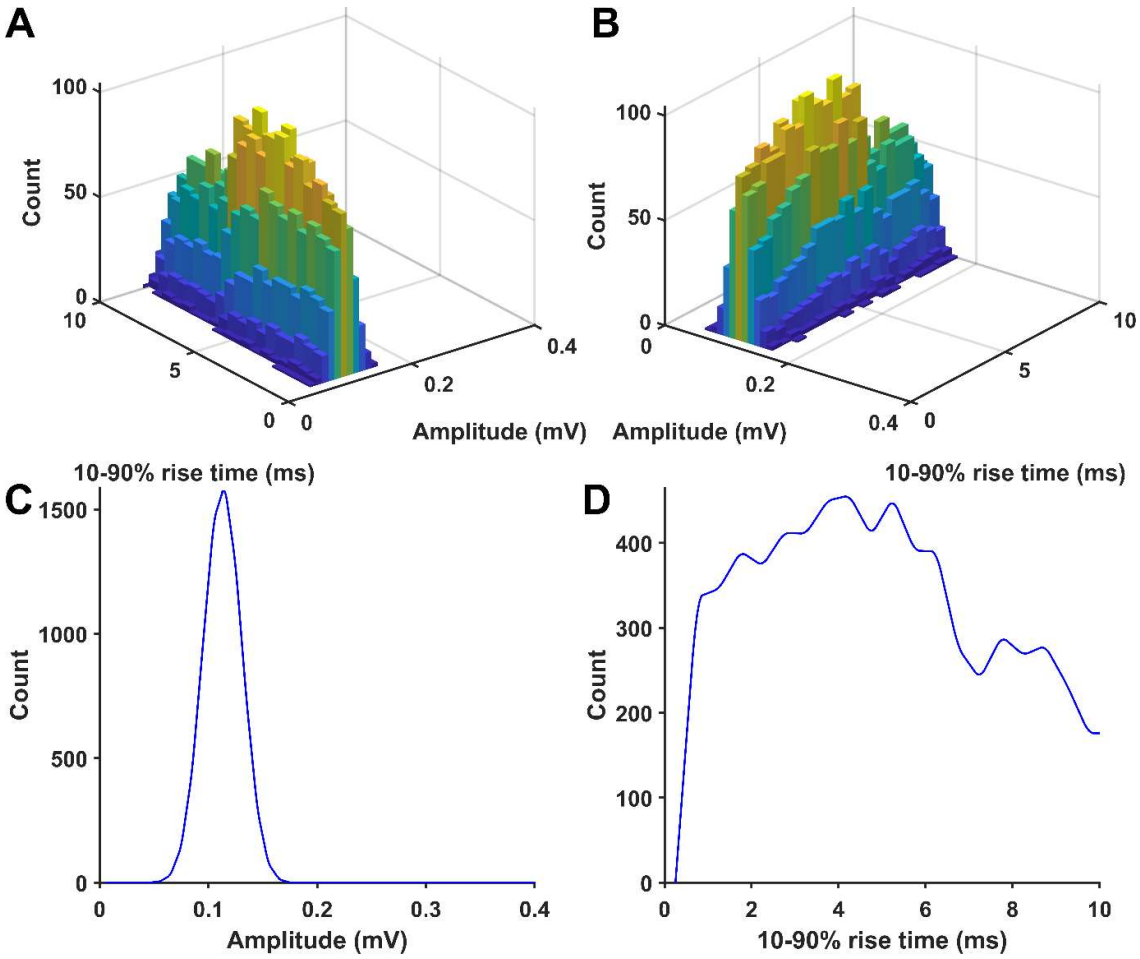

Supplementary figure 27: An example of simulated minis distribution that was used to produce a close match between distributions of detected minis-like events in a 'noise + simulated minis' voltage trace and in a 'noise + real minis' recording for a cell p103a of cortical layer 5.

(A) A joint amplitude and 10-90% rise time distribution of simulated minis.

(B) The same distribution but viewed from a different angle.

(C) Marginal amplitude distribution of the same distribution as in (A).

(D) Marginal 10-90% rise time distribution of the same distribution as in (A).

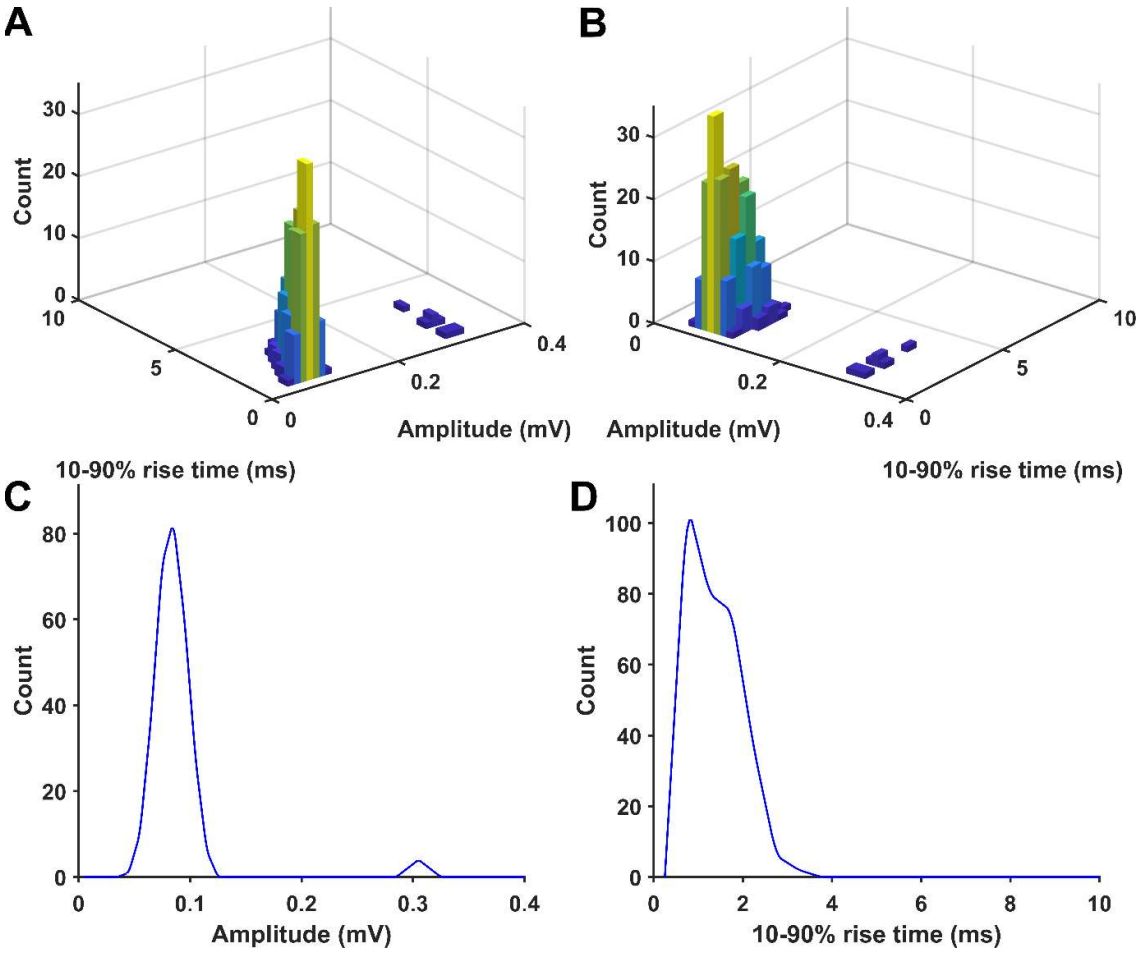

Supplementary figure 28: An example of simulated minis distribution that was used to produce a close match between distributions of detected minis-like events in a ’noise + simulated minis’ voltage trace and in a ’noise + real minis’ recording for a cell p106b of cortical layer 5. The meaning of different figure panels is explained in Supplementary figure 27.

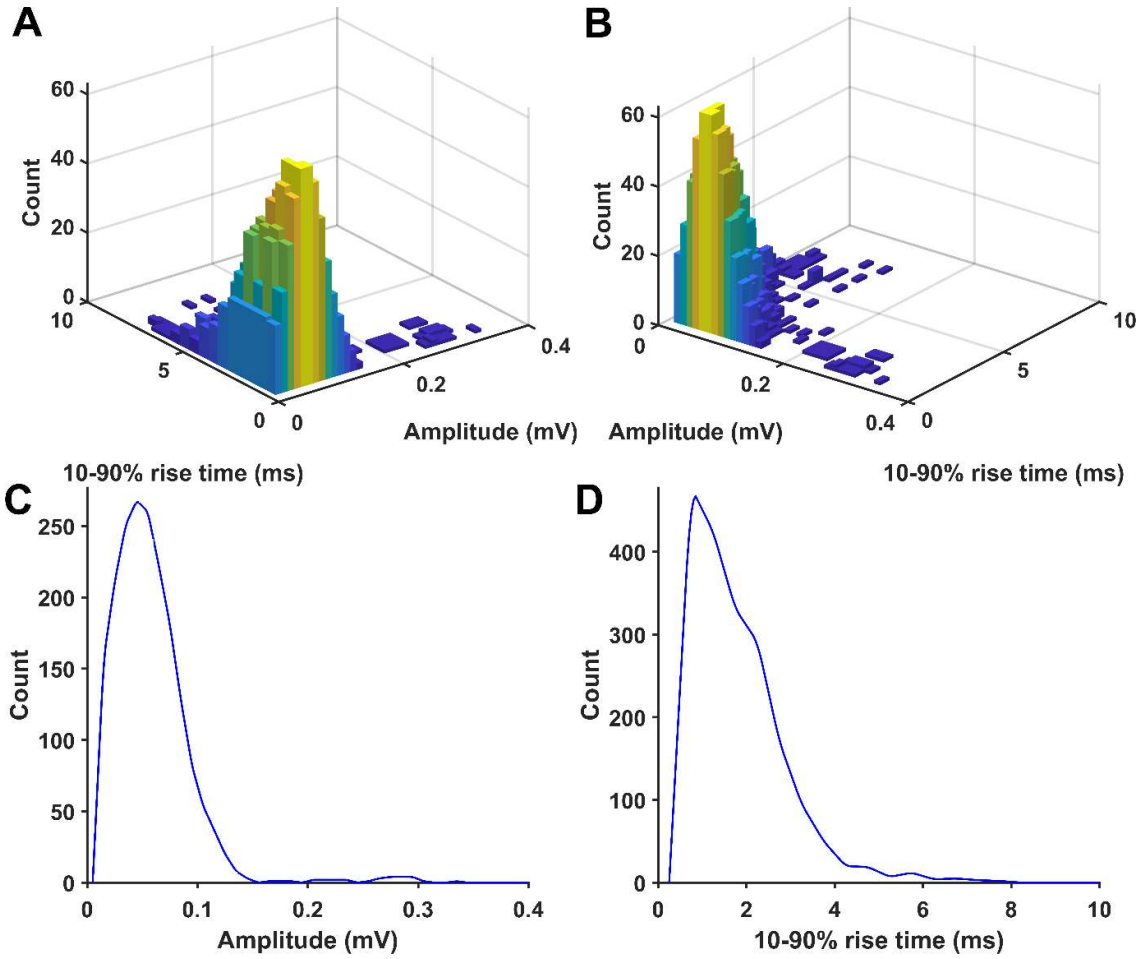

Supplementary figure 29: An example of simulated minis distribution that was used to produce a close match between distributions of detected minis-like events in a ’noise + simulated minis’ voltage trace and in a ’noise + real minis’ recording for a cell p108a of cortical layer 5. The meaning of different figure panels is explained in Supplementary figure 27.

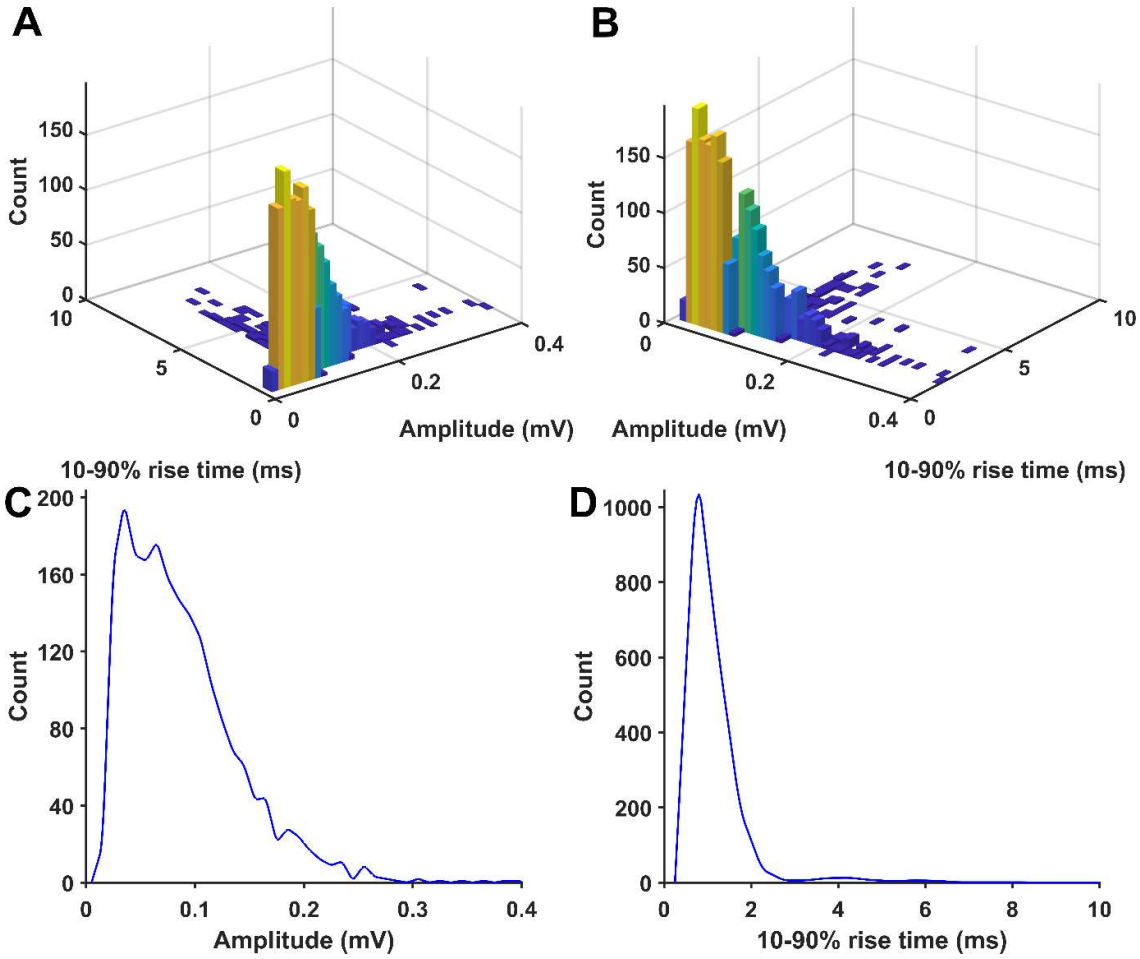

Supplementary figure 30: An example of simulated minis distribution that was used to produce a close match between distributions of detected minis-like events in a 'noise + simulated minis' voltage trace and in a 'noise + real minis' recording for a cell p108b of cortical layer 5. The meaning of different figure panels is explained in Supplementary figure 27.

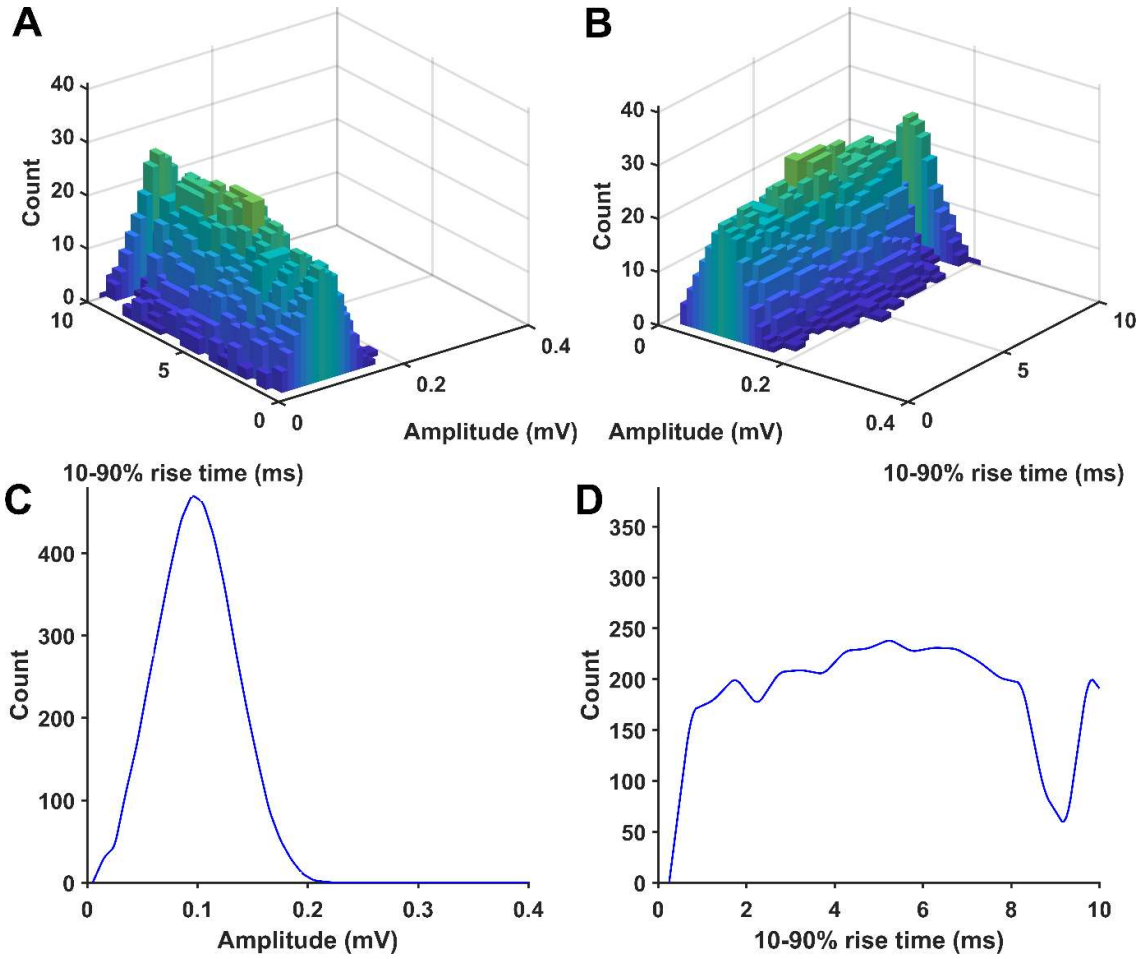

Supplementary figure 31: An example of simulated minis distribution that was used to produce a close match between distributions of detected minis-like events in a ’noise + simulated minis’ voltage trace and in a ’noise + real minis’ recording for a cell p108c of cortical layer 5. The meaning of different figure panels is explained in Supplementary figure 27.

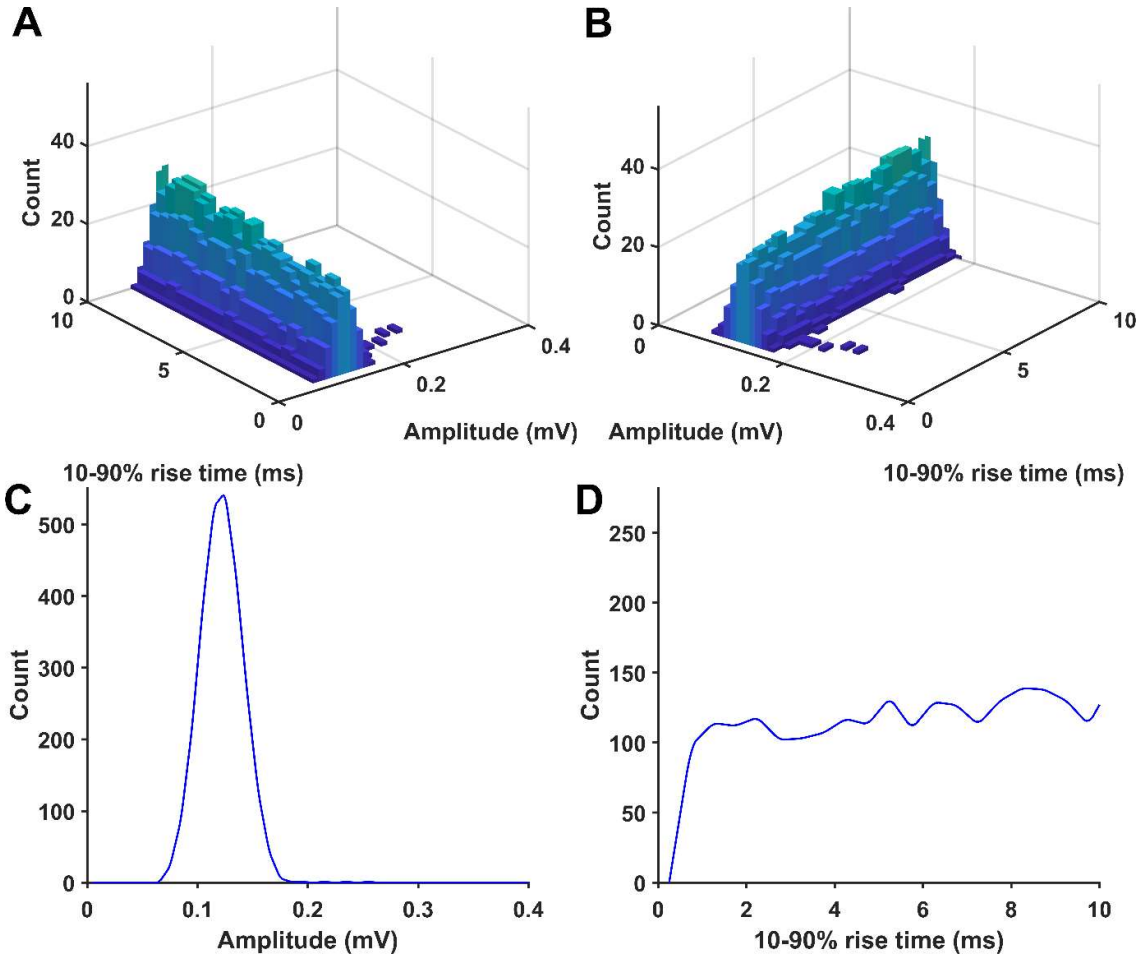

Supplementary figure 32: An example of simulated minis distribution that was used to produce a close match between distributions of detected minis-like events in a ’noise + simulated minis’ voltage trace and in a ’noise + real minis’ recording for a cell p120b of cortical layer 2/3. The meaning of different figure panels is explained in Supplementary figure 27.

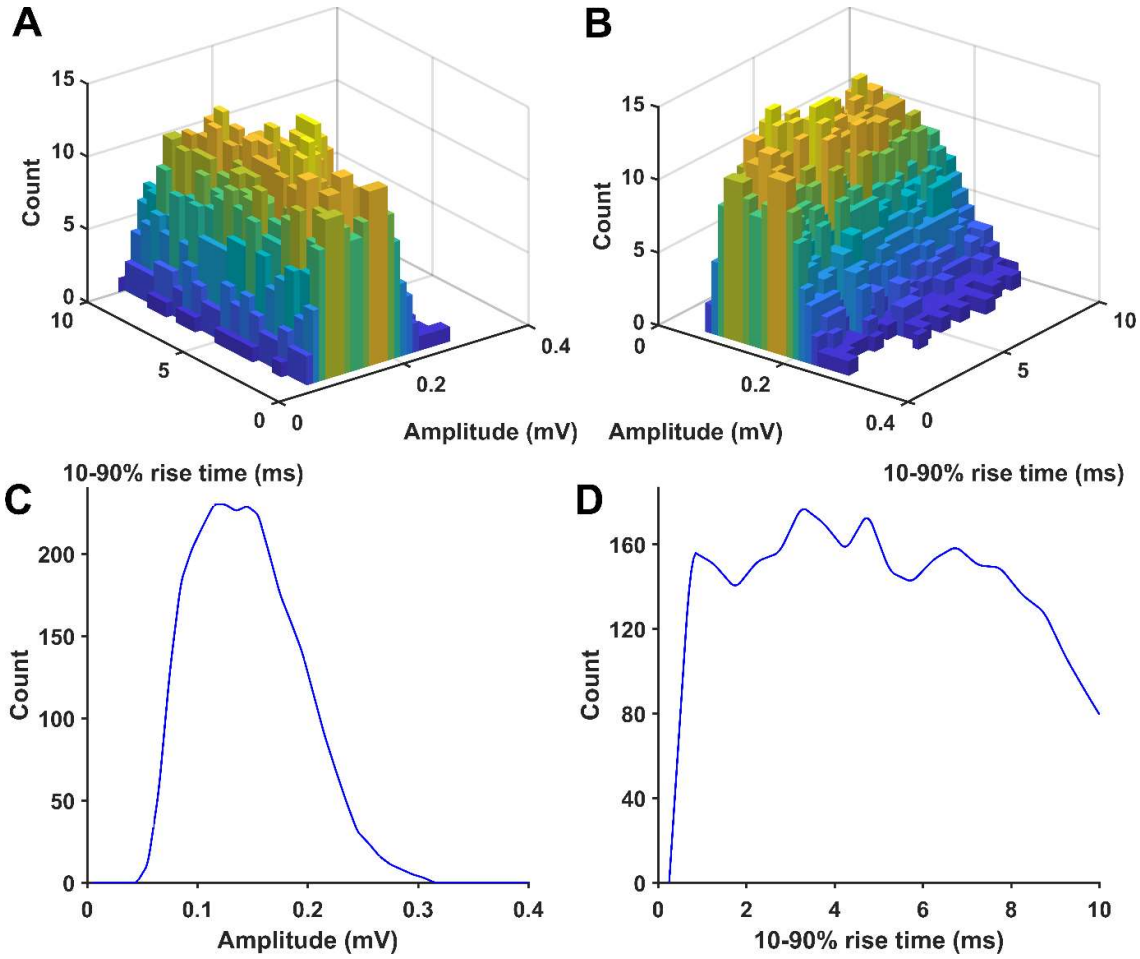

Supplementary figure 33: An example of simulated minis distribution that was used to produce a close match between distributions of detected minis-like events in a 'noise + simulated minis' voltage trace and in a 'noise + real minis' recording for a cell p122a of cortical layer 2/3. The meaning of different figure panels is explained in Supplementary figure 27.

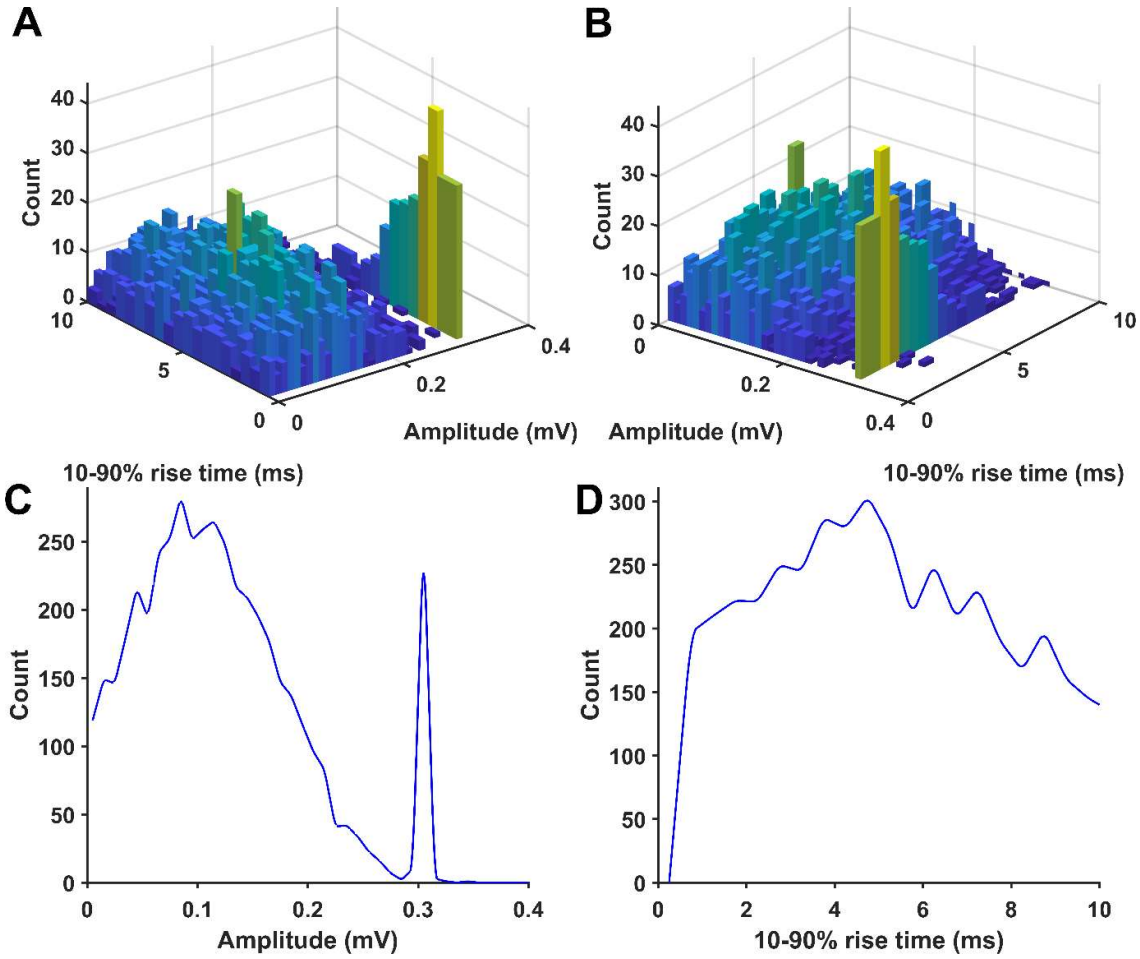

Supplementary figure 34: An example of simulated minis distribution that was used to produce a close match between distributions of detected minis-like events in a 'noise + simulated minis' voltage trace and in a 'noise + real minis' recording for a cell p124b of cortical layer 5. The meaning of different figure panels is explained in Supplementary figure 27.

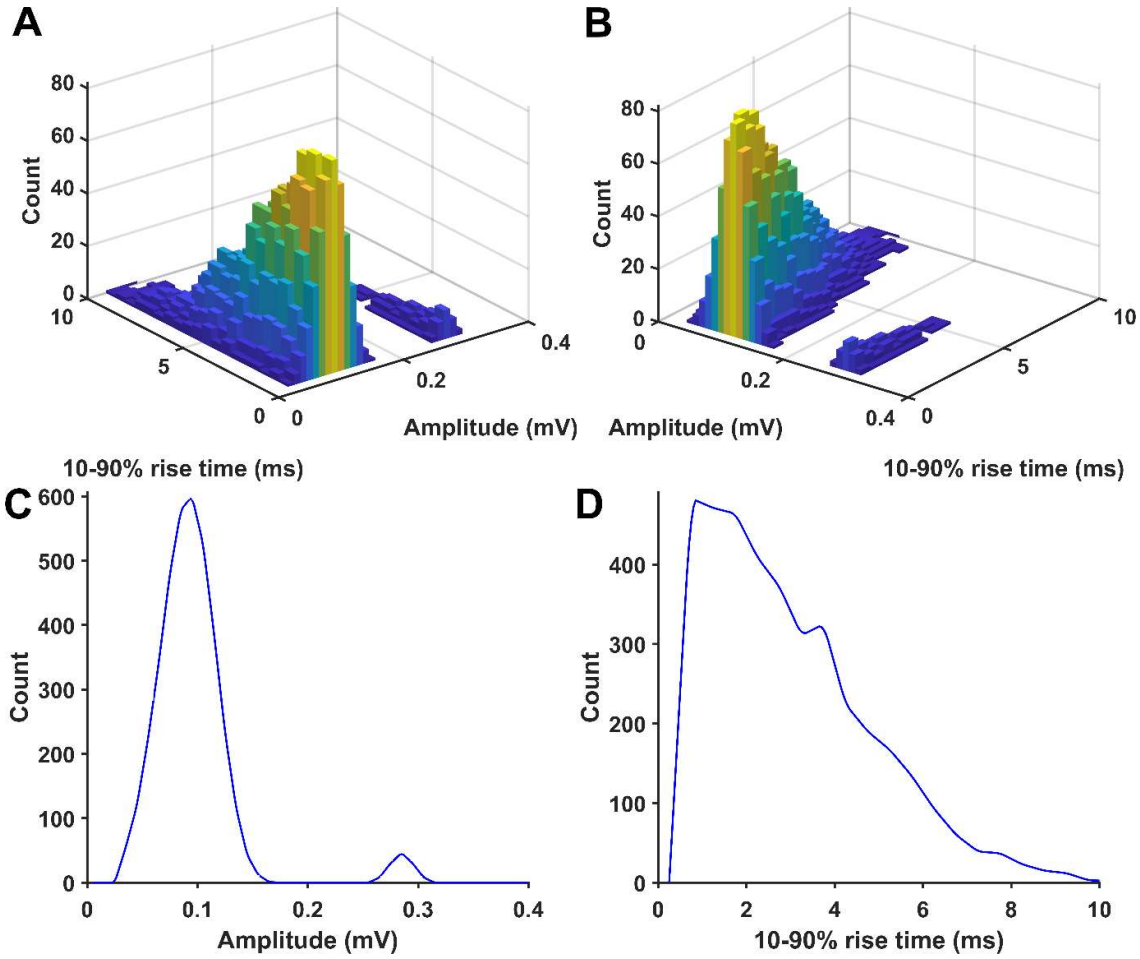

Supplementary figure 35: An example of simulated minis distribution that was used to produce a close match between distributions of detected minis-like events in a ’noise + simulated minis’ voltage trace and in a ’noise + real minis’ recording for a cell p125a of cortical layer 2/3. The meaning of different figure panels is explained in Supplementary figure 27.

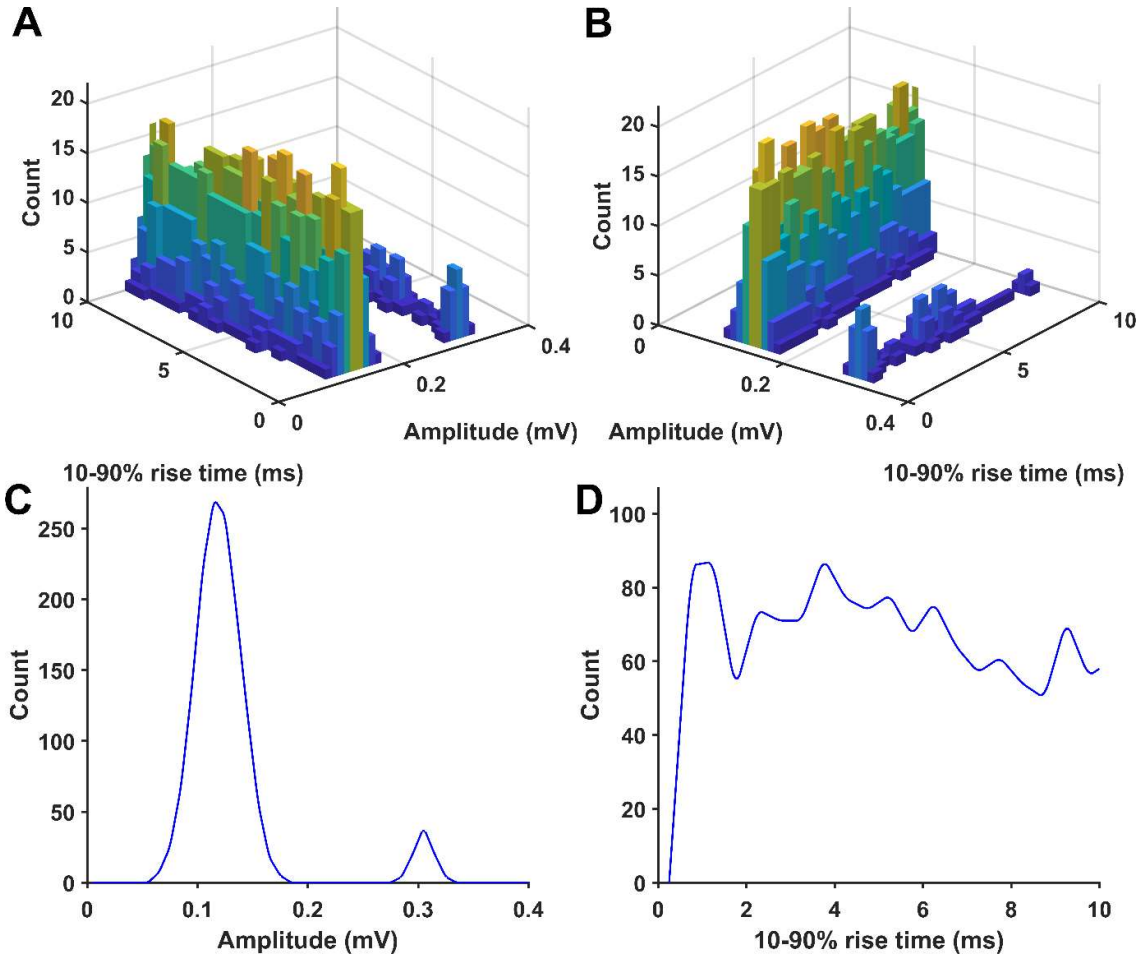

Supplementary figure 36: An example of simulated minis distribution that was used to produce a close match between distributions of detected minis-like events in a ’noise + simulated minis’ voltage trace and in a ’noise + real minis’ recording for a cell p127c of cortical layer 2/3. The meaning of different figure panels is explained in Supplementary figure 27.

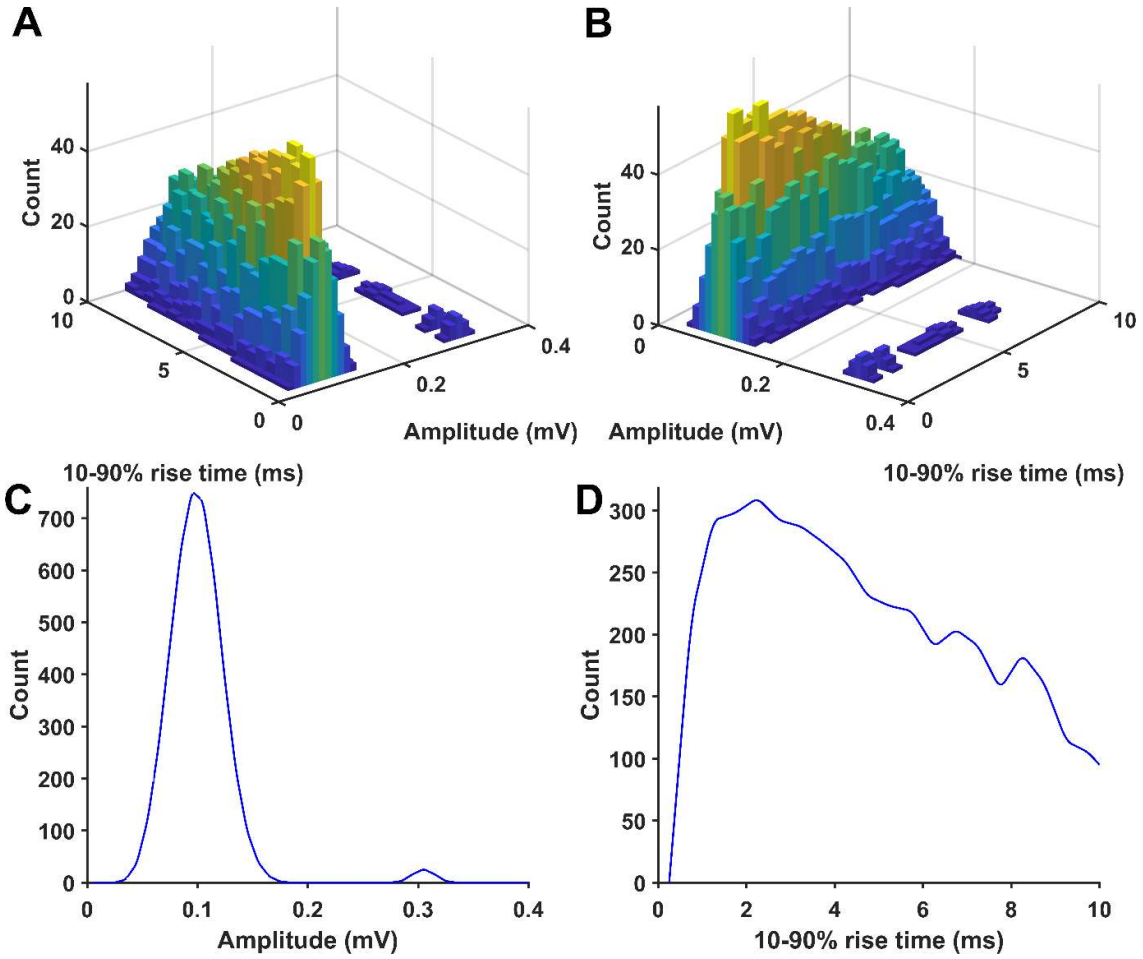

Supplementary figure 37: An example of simulated minis distribution that was used to produce a close match between distributions of detected minis-like events in a ’noise + simulated minis’ voltage trace and in a ’noise + real minis’ recording for a cell p128c of cortical layer 2/3. The meaning of different figure panels is explained in Supplementary figure 27.

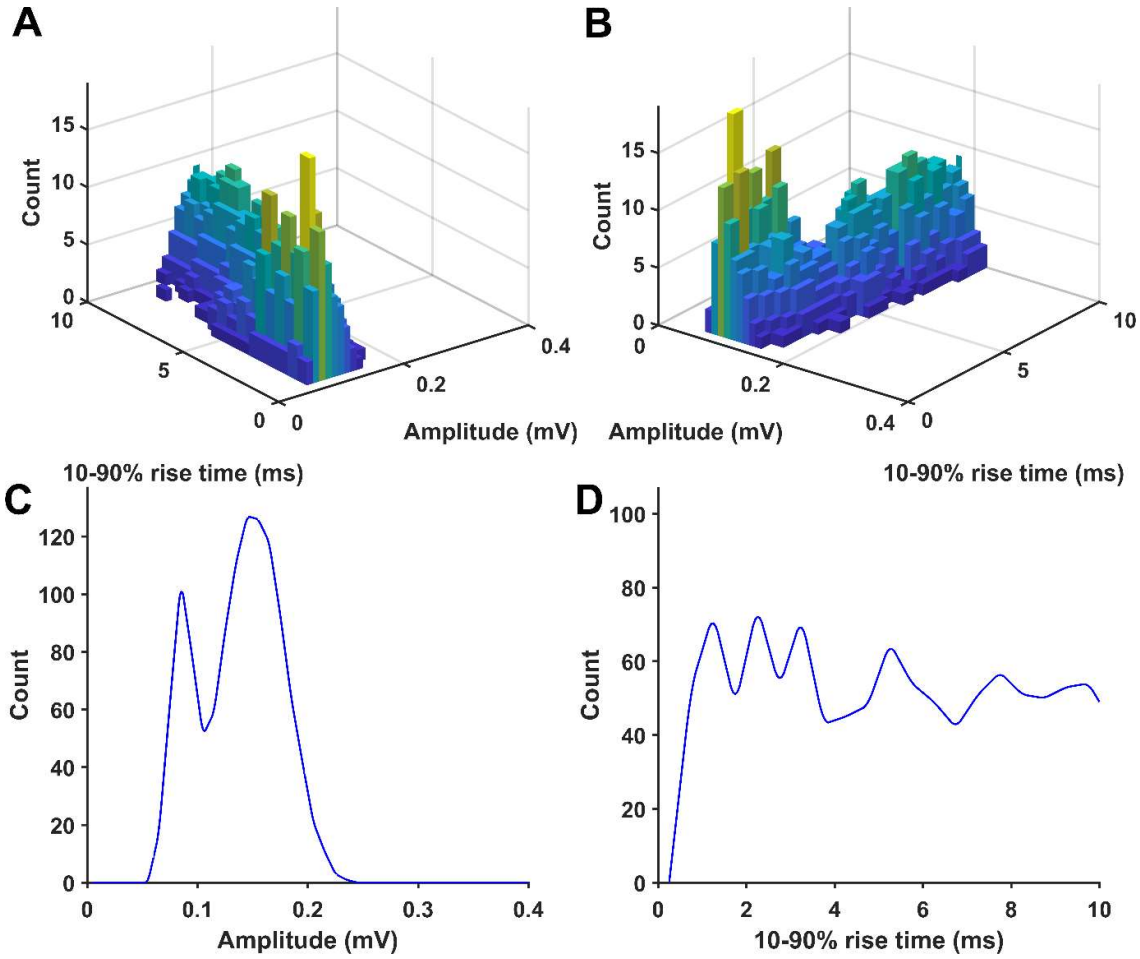

Supplementary figure 38: An example of simulated minis distribution that was used to produce a close match between distributions of detected minis-like events in a ’noise + simulated minis’ voltage trace and in a ’noise + real minis’ recording for a cell p129a of cortical layer 5. The meaning of different figure panels is explained in Supplementary figure 27.

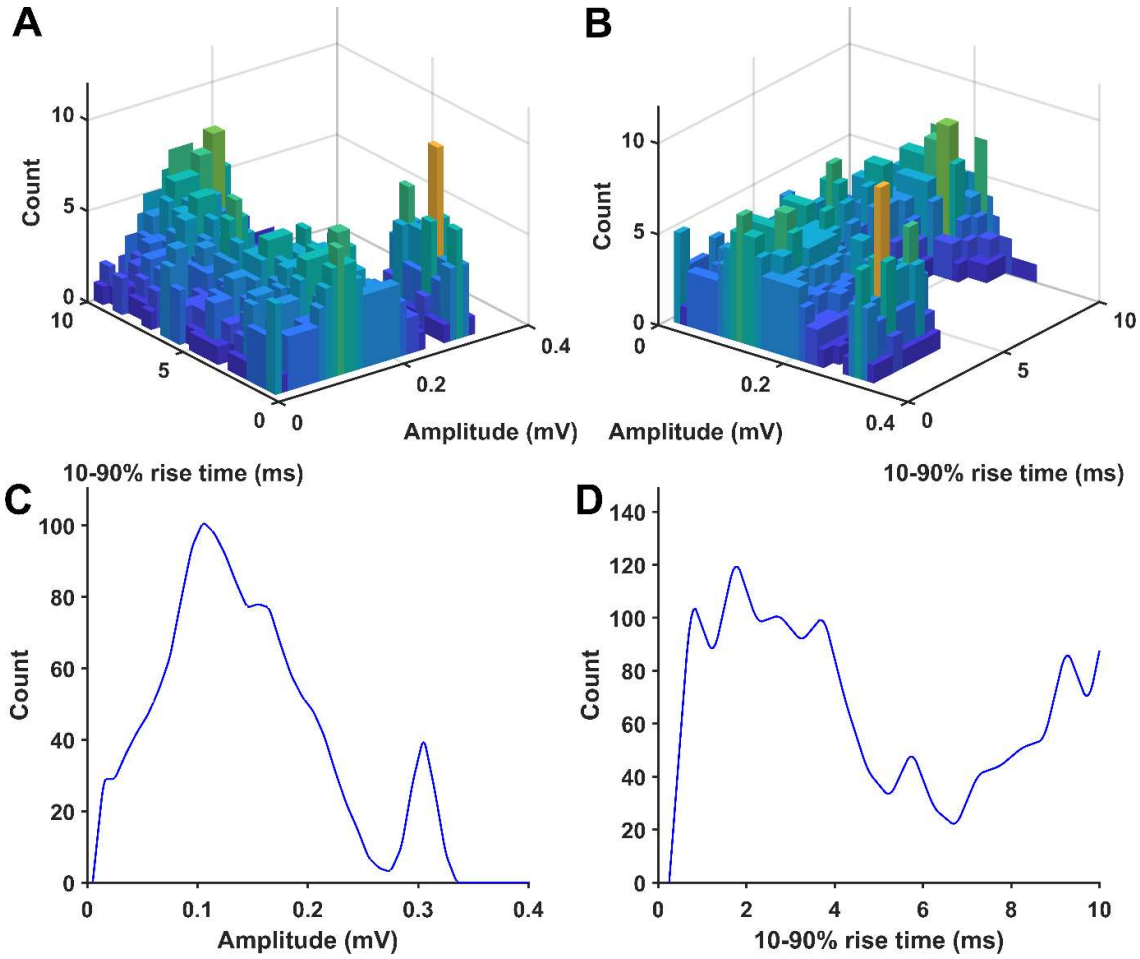

Supplementary figure 39: An example of simulated minis distribution that was used to produce a close match between distributions of detected minis-like events in a ’noise + simulated minis’ voltage trace and in a ’noise + real minis’ recording for a cell p131a of cortical layer 2/3. The meaning of different figure panels is explained in Supplementary figure 27.